Chlamydomonas Mutants Null for Chloroplast Triose Phosphate Transporter3 are Metabolically Compromised and Light Sensitive

Weichao Huang (黄伟超)[1]†*, Anagha Krishnan[2]†, Anastasija Plett[3], Michelle Meagher[4], Nicole Linka[3], Yongsheng Wang[1,5], Bijie Ren[1], Justin Findinier[1], Petra Redekop[1], Neda Fakhimi[1], Rick G. Kim[1], Devin A. Karns[2], Nanette Boyle[4], Matthew C. Posewitz[2], Arthur R. Grossman[1]*

[1]Department of Plant Biology, Carnegie Institution for Science, Stanford, CA 94305, USA

[2]Department of Chemistry, Colorado School of Mines, Golden, CO 80401, USA

[3]Institute of Plant Biochemistry, Heinrich-Heine University Düsseldorf, 40225 Düsseldorf, Germany

[4]Department of Chemical and Biological Engineering, Colorado School of Mines, Golden, CO 80401, USA

[5]School of Life Sciences, Tsinghua University, 100084 Beijing, China

†Authors contributed equally.

*Corresponding Author: Weichao Huang; Address: The Carnegie Institution for Science, 260 Panama St. Bldg. 100; Stanford, CA 94305; email: whuang@carnegiescience.edu

*Corresponding Author: Arthur R. Grossman; Address: The Carnegie Institution for Science, 260 Panama St. Bldg. 100; Stanford, CA 94305; email: agrossman@carnegiescience.edu

Key words: TPT3, reactive oxygen species, CRISPR-Cas9, photosynthetic activity, starch accumulation, redox shuttles

Abstract

Modulation of export of photoassimilates from the chloroplast is essential for controlling the distribution of fixed carbon in the cell and maintaining optimum photosynthetic rates. In this study we identified chloroplast triose phosphate/phosphate translocators 2 and 3 (CreTPT2 and CreTPT3) in the green alga *Chlamydomonas reinhardtii* that exhibited similar substrate specificities but were differentially expressed over the diel cycle. We focused mostly on analyzing CreTPT3 because of its high level of expression and the severe phenotype exhibited by *tpt3* relative to the *tpt2* mutants. Null mutants for CreTPT3 had a pleiotropic phenotype that impacted growth, photosynthetic activities, metabolite profiles, carbon partitioning, and organelle-specific accumulation of H_2O_2. These analyses demonstrated that CreTPT3 is a dominant conduit on the chloroplast envelope for the transport of photoassimilate. In addition, CreTPT3 can serve as a safety valve that moves excess reductant out of the chloroplast and appears to be essential for preventing the cells from experiencing oxidative stress and accumulating of reactive oxygen species, even under low/moderate light intensities. Finally, our studies indicate subfunctionalization of the CreTPT transporters and suggest that there are differences in managing the export of photoassimilates from the chloroplasts of Chlamydomonas and vascular plants.

Introduction

Photosynthetic organisms can absorb excess, potentially damaging levels of light energy during mid-day (when photosynthetic electron transport becomes saturated) and can suffer from extreme damage, especially when experiencing rapid fluctuations in light intensities or when subjected to nutrient limiting conditions and other environmental stresses that impair the productive utilization of excitation energy (Chaux et al., 2017; Saroussi et al., 2017). To cope with excess excitation energy, plants and algae have evolved mechanisms to dissipate this energy through nonphotochemical quenching (NPQ) (Niyogi and Truong, 2013). The excess reductant and energy can also be eliminated by photochemical quenching. While the dominant form of photochemical quenching often involves the use of the electrons/reductant to fix inorganic carbon (Ci), which is directed toward growth or stored in the form of starch and lipids (Krishnan et al., 2015; Ge et al., 2014; Huang et al., 2018), redox equivalents can also be trafficked to other outlets where they are not used for anabolic processes. The main alternative photochemical electron outlets involve the reduction of O_2 to H_2O in H_2O-to-H_2O cycles that include a (*i*) Mehler-type reaction that is noncatalytic and functions on the acceptor side of PSI (Badger et al., 2000), (*ii*) flavodiiron protein reactions (FLVs, NADPH:flavin oxidoreductase) that catalytically reduce O_2 on the acceptor side of PSI without generating reactive oxygen species (ROS) (Helman et al., 2003; Chaux et al., 2017), (*iii*) the plastid terminal oxidase (PTOX, plastoquinol: oxygen oxidoreductase) reaction that can use electrons from the PQ pool to reduce O_2 (Houille-Vernes et al., 2011), and (*iv*) the movement of redox equivalents from the chloroplast to the mitochondrion where they can be used to reduce O_2 through various electron transport activities.

Mechanisms also exist in which fixed carbon and reducing equivalents can be shuttled between the chloroplast and cytoplasm. Studies with *Arabidopsis thaliana* revealed that the malate shuttle, which involves multiple malate dehydrogenases (MDH) and malate/OAA translocators (OMT), functions in the export of reductant from the chloroplast and the management of redox conditions in the chloroplast (Zhao et al., 2020, 2018). In addition to the malate shuttle, the triose phosphate (triose-P)/phosphate (Pi) translocator (TPT) has been proposed to be involved in moving fixed carbon out of the chloroplast, but can also act as a safety valve for eliminating excess reducing power from the chloroplast (Fliege et al., 1978; Flügge et al., 1989; Lee et al., 2017; Stocking and Larson, 1969; Raghavendra and Padmasree, 2003; Johnson and Alric, 2013). The synthesis of triose-Ps during photosynthetic CO_2 fixation by the Calvin-Benson-Bassham Cycle (CBBC) is

supported by the reducing power/energy (NADPH, ATP) derived from photosynthetic electron transport.

The TPTs reside on the inner chloroplast envelope membrane and can transport triose-Ps (glyceraldehyde 3-phosphate (GAP), dihydroxyacetone phosphate (DHAP)) and the three carbon acid 3-phosphoglycerate (3-PGA) in a counter exchange for cytosolic Pi (Fliege et al., 1978; Lee et al., 2017; Flügge et al., 1989). These transporters belong to a family of plastidic phosphate translocators (pPTs) that function as antiport systems involved in exchanging Pi with phosphorylated C3, C5 or C6 compounds (Flügge et al., 2003). Most angiosperms have two *TPT* genes in their genome, except for various monocots and two dicot families, the Amaranthaceae and the Brassicaceae, which have a single *TPT* gene (Bockwoldt et al., 2019). In plants, cytosolic trioses exported from the chloroplast by the TPTs are used for the biosynthesis of sucrose and other metabolites (Riesmeier et al., 1993) and to drive respiratory activity. In addition to TPTs, plants harbor the three other pPT subfamilies (Fischer et al., 1997; Kammerer et al., 1998; Eicks et al., 2002; Lee et al., 2017; Flügge et al., 1989). These include the glucose 6-phosphate (Glc6P) translocator (GPT), which imports Glc6P into plastids in heterotrophic tissue (Kammerer et al., 1998), the xylulose phosphate translocator (XPT), which plays a key role in coordinating the cytosolic and plastidic pentose phosphate pathways (Eicks et al., 2002), and the phosphoenolpyruvate (PEP) translocator (PPT), which imports PEP into C3 plastids; the PEP can be used for the synthesis of fatty acids, as substrate for the shikimate pathway (Streatfield et al., 1999; Prabhakar et al., 2010), and for the export of PEP from plastids in C4 plants (Häusler et al., 2000).

Over the last few decades, the physiological functions of the TPTs have been examined in some detail. Various plants do not exhibit a strong phenotype if the chloroplast TPT is either eliminated or its level is reduced (Häusler et al., 1998; Walters et al., 2004; Schneider et al., 2002; Riesmeier et al., 1993). A reduction in TPT activity can be compensated for by diverting assimilated carbon into a transitory starch pool that is subjected to accelerated turnover in the light and/or dark (Häusler et al., 1998; Walters et al., 2004; Riesmeier et al., 1993), leading to accumulation of starch degradation products that can be exported from the chloroplast and used in other cellular compartments. Interestingly, a deficiency of the TPT in rice, a plant that uses sucrose stored in the leaves as its major transitory form of fixed carbon, led to severe phenotypic consequences; the plants exhibited reduced photosynthetic rates and decreased levels of both starch and soluble

103 sugars relative to wild type (WT) plants (Lee et al., 2014).

104 Microalgae have high photosynthetic conversion efficiencies, can thrive in fresh to hypersaline
105 waters and can be metabolically versatile. They have attracted considerable interest worldwide
106 because of their ability to synthesize large quantities of lipids (e.g. for biofuels and food products),
107 starch, pigments and other bioproducts, and can serve in the remediation of wastewater (Khan et
108 al., 2018; Bhatt et al., 2022). The transporters used for moving photoassimilate between the
109 chloroplast and other cellular compartments and the mechanisms and regulation of these
110 transporters in microalgae have not been extensively explored. Developing a more informed
111 understanding of central metabolism in microalgae and the movement of metabolites among
112 compartments can enable additional work on the establishment, regulation, and evolution of
113 metabolic networks in algae and the ways in which algae can be tailored for production purposes
114 and for sustained growth under specific environmental conditions.

115 In this study, we used Chlamydomonas, a well-established model green algal system that has been
116 extensively used to analyze various physiological processes, to dissect the function of chloroplast
117 TPTs. Of the four putative Chlamydomonas pPTs, we discovered that at least two are 'genuine'
118 TPTs (CreTPT2 and CreTPT3) based on yeast liposome transport assays. CreTPT2 was previously
119 reported to be a PPT based on phylogenetic analysis (Bockwoldt et al., 2019). These two TPTs
120 exhibited sub-functionalization that is reflected by their expression levels and temporally and
121 environmentally distinct regulatory patterns. Due to the more severe phenotypes exhibited by *tpt3*
122 relative to *tpt2* mutants, we focused our analyses on Chlamydomonas TPT3 (CreTPT3) which,
123 among the four predicted pPTs, is highly expressed in the light and strongly induced by various
124 environmental stresses. Through a series of physiological analysis, we demonstrated that CreTPT3
125 is a major conduit on the chloroplast envelope for the trafficking of fixed carbon, sustaining central
126 carbon metabolism, dissipating excess energy, enabling high rates of photosynthetic electron
127 transport, preventing intracellular hydrogen peroxide (H_2O_2) accumulation, and balancing redox
128 conditions at the subcellular level.

129 **Results**

130 **The triose-P/Pi translocator (DMT/TPT) family**

131 Candidate genes encoding triose-P/Pi transporters (TPT) of Chlamydomonas were identified by

132 blasting the Arabidopsis TPT protein (AT5G46110.1) against proteins encoded on the
133 Chlamydomonas genome. The TPT family is the largest within the drug/metabolite transporter
134 (DMT) superfamily in eukaryotes and includes triose-P and sugar-phosphate transporters
135 associated with chloroplasts; many of the family members are still not functionally characterized
136 (Jack et al., 2001; Knappe et al., 2003; Weber et al., 2006). We identified 32 genes encoding
137 potential TPTs in the version v6.1 genome of Chlamydomonas, with four members, CreTPT10
138 (CreTPT1 in v5.6 genome), CreTPT2 (CreTPT2 in v5.6 genome), CreTPT3 and CGL51
139 (CreTPT25 in v5.6 genome), predicted to have a transit peptide that would localize the protein to
140 the chloroplast (**Supplementary Table 1**). These four candidates were included in a phylogenetic
141 analysis of plant and algal pPTs that showed that CreTPT3 is a putative TPT, CreTPT2 and
142 CreTPT10 are putative PPTs, and CGL51 is a putative GPT or XPT (Bockwoldt et al., 2019).

143 To examine the potential substrate specificities of the four putative pPTs, their amino acid
144 sequences were aligned with pPTs from Arabidopsis (AtPTs) (**Supplementary Fig. 1A**). The
145 ability of these transporters to use triose-P/DHAP or 3-PGA as substrate is dependent on five
146 highly conserved amino acid residues (H184, K203, Y338, K359, and R360 in AtTPT1) (Lee et
147 al., 2017; Moog et al., 2020). Of the putative pPTs in Chlamydomonas, only CreTPT3 and CGL51
148 contain all five of these residues (H170, K189, Y322, K345, and R346 in CreTPT3)
149 (**Supplementary Fig. 1A**). In AtTPT1, residue F262 (F248 in Chlamydomonas in the analogous
150 protein, CreTPT3) is thought to inhibit PEP access to the binding site; this residue is replaced by
151 N in AtPPT1 (PPT) (Lee et al., 2017; Moog et al., 2020). CGL51 has an M at position F248,
152 indicating that unlike CreTPT3, CGL51 might have preference for other substrates. Protein
153 sequence similarity and identity analysis show CreTPT3 and CreTPT2 share the highest and the
154 second highest similarity and identity with AtTPT1, (**Supplementary Fig. 1B**) and are 57% and
155 49% similar to AtTPT1, respectively. Furthermore, *CreTPT2* and *CreTPT3* have significantly
156 higher transcript accumulation in light relative to Cre*TPT10* and *CGL51* (**Supplementary Fig. 1C,**
157 **D**). Given the high similarity and high expression levels, CreTPT2 and CreTPT3 were chosen for
158 further study.

159 **CreTPT2 and CreTPT3 transport properties**

160 We defined the subcellular localization and substrate preferences of both CreTPT2 and CreTPT3.
161 As shown in **Fig. 1A**, both CreTPT2 and CreTPT3 fused to VENUS localized to the chloroplast

162 envelope. To evaluate the substrate specificity of these transporters, each of them was expressed
163 in *Saccharomyces cerevisiae* (yeast) and the resulting recombinant protein was biochemically
164 analyzed using a liposome uptake assay. The Cre*TPT2* and Cre*TPT3* genes were fused at their C
165 termini to a sequence encoding a His tag, codon-optimized, and expressed in yeast (**Fig. 1B**), and
166 total cell membranes were isolated and reconstituted into liposomes (Loddenkötter et al., 1993;
167 Linka et al., 2008). Chloroplast phosphate transporters in vascular plants can catalyze a Pi/Pi
168 homo-exchange in vitro. Both CreTPT2 and CreTPT3 reconstituted in liposomes were able to
169 catalyze the signature Pi homo-exchange, whereas in the absence of a counter-exchange substrate,
170 little Pi uptake was detected (**Fig. 1C** and **D**, left). In contrast, very low Pi uptake rates were
171 observed for liposomes reconstituted with membranes from yeast cells lacking CreTPT2 or
172 CreTPT3 (**Supplementary Fig. 2**), indicating that the introduced transporters were responsible for
173 the detected Pi import activity in the yeast liposomes.

174 To assess the substrate specificity of the CreTPT transporters, the initial rates of Pi uptake into
175 liposomes preloaded with saturating concentrations (30 mM) of various potential counter-
176 exchange substrates were determined. As the right panels of **Fig. 1C** and **D** show, both CreTPT2
177 and CreTPT3 exhibited the highest activity when DHAP was used as the substrate for the yeast
178 liposome assay. For both transporters, the relative initial velocity for DHAP/Pi exchange was
179 slightly higher than that of 3-PGA/Pi (the relative 3-PGA/Pi exchange was 75% of DHAP/Pi
180 exchange) while Pi uptake into liposomes preloaded with PEP was much lower (**Fig. 1C** and **D**,
181 right panels). Pi import was negligible when CreTPT2 or CreTPT3 liposomes were preloaded with
182 Glc-6-P, Glc-1-P, Fru-6-P, and Gal-1-P (**Fig. 1C** and **D**, right panels). These results show that
183 CreTPT2 and CreTPT3 have almost the same substrate preferences, with both specifically
184 catalyzing the transport of triose-P and 3-PGA across the membrane in exchange for Pi.

185 Characterizations of the K_M and K_i for CreTPT2 and CreTPT3 were performed to determine the
186 affinity of these transporters for the various substrates. CreTPT3 has an apparent Michaelis-
187 Menten constant (K_M) of 1.1 +/- 0.2 mM for Pi (**Fig. 1E**), which is comparable to the value
188 obtained for the vascular plant TPT ortholog (Fliege et al., 1978). CreTPT2 has a slightly lower
189 K_M for Pi than CreTPT3 (0.77 +/- 0.05 mM) (**Fig. 1E**). However, while the 3-PGA Ki values were
190 comparable for the two transporters, DHAP was more effective in inhibiting the CreTPT3-
191 dependent Pi exchange than CreTPT2-dependent Pi exchange (**Fig. 1E**). These results suggest that

192 CreTPT3 may have a greater specificity for the transport of DHAP than CreTPT2 and that it may
193 be more effective in transporting C3 phosphorylated compounds than CreTPT2. In the case of
194 PEP, no inhibition of the Pi/Pi homo-exchange was observed, even at the non-physiologically high
195 concentration of 5 mM. Overall, the results of these in vitro assays indicate that both CreTPT2 and
196 CreTPT3 have a typical plant-TPT substrate spectrum (Fliege et al., 1978) and can transport Pi,
197 triose-P (DHAP) and 3-PGA in a counter-exchange mode. However PEP might not be a
198 physiologically relevant substrate for either CreTPT2 or CreTPT3, as was shown for apoplast TPT
199 homologues in other organisms (Lim et al., 2010; Moog et al., 2020). Furthermore, the values
200 generated in these analyses may not precisely reflect transport kinetics in vivo since the two
201 transporters used for these in vitro assays were fused to a His-tag at their N terminus, and the yeast
202 liposomes would have a different lipid composition than the chloroplast inner envelop membrane,
203 where these transporters are normally localized.

204 **Isolation of *tpt2* and *tpt3* null mutants of Chlamydomonas and their impacts on cell growth**

205 To explore the role of CreTPT2 and CreTPT3 in trafficking carbon and potentially reductant across
206 the chloroplast envelope in vivo, CRISPR knockouts of Cre*TPT2* or Cre*TPT3* were generated. We
207 used the CRISPR-Cas9 editing system to disrupt the Cre*TPT2* or Cre*TPT3* genes while at the same
208 time integrating the hygromycin resistance marker gene (*AphVII*) into the edited site (**Fig. 2A,**
209 **Supplementary Fig. 3** and **4**). Four independent knockouts of Cre*TPT2* (*t2ko1, t2ko2, t2ko3 and*
210 *4*) were obtained, with the marker gene inserted into exon 8 (**Supplementary Fig. 3)**. Three
211 independent knockouts of Cre*TPT3* were obtained, including *t3ko1*, with the marker gene inserted
212 into exon 1, and *t3ko2* and *t3ko3*, with the marker gene inserted into exon 7; no CreTPT3 protein
213 was detected in any of these edited strains (**Fig. 2B**).

214 To elucidate the physiological roles of CreTPT2 and CreTPT3, we first examined growth of the
215 parental WT strain and the knockout mutants under either low light (LL, 30 µmol photons m^{-2} s^{-}
216 ^{1}), moderate light (ML, 250-300 µmol photons m^{-2} s^{-1}) or high light (HL, 450 µmol photons m^{-2} s^{-}
217 ^{1}). The design of the experiments in which the cells were transferred from one light condition to
218 another is shown in **Supplementary Fig. 5**. The four *tpt2* mutants (*t2ko1, t2ko2, t2ko3 and 4*) were
219 not impacted by growth in LL, but their growth was significantly impaired relative to WT cells
220 under HL on either photoautotrophic (TP) or heterotrophic (TAP) solid agar medium
221 (**Supplementary Fig. 3D, Fig. 2C**). In contrast, the Cre*TPT3* mutants (*t3ko1, t3ko2* and *t3ko3*)

222 exhibited severe growth impairment even in LL, and completely stopped growing under ML and
223 HL, on either TP or TAP agar medium (**Fig. 2C, D**). Due to the striking growth phenotypes caused
224 by the loss of CreTPT3, we focused on investigating the physiological functions of TPT3 by
225 analyzing *tpt3* mutants in more detail in this study. The differences in transcript changes between
226 Cre*TPT2* and Cre*TPT3* under various environmental conditions were examined and are described
227 in the 'Discussion' section.

228 Growth curves were also determined for WT and *tpt3* mutant cells in liquid medium (TP) in LL,
229 ML and HL (**Fig. 2E** and **2F**); the results were in accord with those observed for the solid medium
230 growth assays. Additionally, *tpt3* mutant cells in both LL and ML exhibited an increased cell
231 diameter and formed clusters of cells that appear to be less able to separate following cell division
232 (**Supplementary Fig. 6A**, **B**). To further confirm that the growth phenotypes are a consequence
233 of the *tpt3* knockout, we introduced a wild-type copy of Cre*TPT3* fused to VENUS into the mutant
234 strains (**Fig. 2B**, right). As shown in **Fig. 2D-G**, ectopic expression of the wild-type Cre*TPT3* in
235 the *t3ko2* mutant (*C_T3KO2*) rescued the reduced growth phenotype of the mutant under all light
236 conditions tested in this study (LL/ML/HL).

237 We also analyzed the chlorophyll content of photoautotrophically grown cells after transferring
238 them from LL to ML and found that *t3ko2* had reduced chlorophyll content relative to WT cells
239 after 24 h in ML (**Fig. 2F-G** and **Supplementary Fig. 7**). Cell numbers and total chlorophyll were
240 quantified following the LL to ML transition. The chlorophyll levels per cell declined in all strains
241 at 24 and 48 h following transfer to ML; however, it was lower by approximately half in *t3ko2*
242 (0.34 μg/10^6 cells) relative to either WT cells or the *C_T3KO2* rescued strain (both ~0.72 μg/10^6
243 cells) after 24 h of ML (**Supplementary Fig. 7**), with some additional increase in cell density for
244 WT and *C_T3KO2* after 48 h of ML (which might result in some shading). Finally, when mutant
245 cells were transferred to HL for 24 h they became strongly bleached (**Fig. 2F**).

246 Taken together, these results indicate that the activity of the CreTPT3 transporter is essential for
247 optimal growth over a range of light intensities (LL/ML/HL).

248 **The *tpt3* mutant exhibits hyper-accumulation of 'storage' carbon**

249 To explore the impact of the loss of CreTPT3 activity on carbon partitioning, we quantified carbon
250 storage (starch and lipids) following a transition of WT and the *t3ko2* mutant from LL to ML.

251 Lugol staining showed extensive starch accumulation in the *t3ko2* cells after a 48-h exposure to
252 ML, whereas WT cells were barely stained (**Fig. 3B**). Furthermore, as shown in **Fig. 3A**, there is
253 a ~55-fold difference in the level of starch that accumulated in *t3ko2* relative to WT cells (13.29
254 compared to 0.24 µg starch/µg chlorophyll, respectively) after 24 h of illumination in ML. The
255 mutant also accumulated ~24-fold more lipid than WT and *C_T3KO2* cells (on a chlorophyll basis),
256 as monitored by Nile Red fluorescence, over the same time period (WT and *t3ko2*: 1038 and 41
257 Nile Red fluorescence/chlorophyll, respectively) (**Fig. 3C, D**). Since the chlorophyll in the mutant
258 on a per cell basis was approximately 50% relative to that of WT cells after 24 h in ML, the
259 accumulated starch and lipid on a per cell basis would be ~25-fold more starch and ~12-fold more
260 lipid in the mutant relative to the WT strain. Additionally, mutant cells are much larger and tended
261 to exhibit more aggregation than WT cells (**Supplementary Fig. 6A, B**). These results suggest
262 that the inability to transport triose-P between the chloroplast and the cytosol through CreTPT3
263 resulted in a repartitioning of photosynthetic assimilates (carbon, reductant, and ATP) toward the
264 synthesis of both starch and neutral lipid.

265 **Cre*TPT3* deletion leads to accumulation of CBBC/glycolytic/gluconeogenic intermediates**

266 To understand the metabolic consequences of the loss of CreTPT3 on growth under LL and ML,
267 comparative metabolite analyses of WT and the *t3ko2* mutant were performed on cells grown in
268 LL and after shifting them to ML for both 45 min and 6 h. As mentioned above, the level of starch
269 increased dramatically in the mutant relative to WT cells (**Fig. 3A, B** and **Supplementary Fig.**
270 **8A**). Pool sizes of various central carbon metabolites, particularly those of the
271 CBBC/glycolysis/gluconeogenesis pathways and intermediates of the TCA/glyoxylate cycle (**Fig.**
272 **3F**), were quantified. Data was normalized to both cell number (**Fig. 3E**) and chlorophyll content
273 (**Supplementary Fig. 8B**). The fold-change in the quantity of each metabolite in the mutant
274 relative to WT under LL or at 45 min and 6 h after the switch to ML is given in **Fig. 3G** and
275 **Supplementary Fig. 8C**.

276 At the time of shifting cells from LL (**Fig. 3E**, time 0 h) to ML, the *t3ko2* mutant had already
277 accumulated a significantly larger pool (2- to 6-fold) of glycolytic/gluconeogenic intermediates
278 [DHAP, 3-PGA, FBP (all three shared with CBBC), G6P, and PEP] compared to WT cells,
279 suggesting that the loss of CreTPT3 resulted in a back-up of these metabolites within the cell; our
280 hypothesis is that these metabolites are accumulating in the chloroplast stroma due to the reduced

281 ability of the mutant chloroplast to export fixed carbon, which is supported by the observed
282 accumulation of starch and TAG in the mutant strain (**Fig. 3A-D** and **Supplementary Fig. 8A**).
283 While the pool sizes of fumarate and malate (metabolites of the TCA/glyoxylate cycle) were
284 similar in both strains under LL, following the transition of the cells to ML, WT cells exhibited a
285 significant increase in the pool sizes of those metabolites while the mutant maintained a lower
286 level, indicating that the loss of CreTPT3 either directly (by supplying precursors) or indirectly
287 (metabolic rewiring) impacts their levels.

288 Thus, a primary function of CreTPT3 appears to be the export of photosynthetically synthesized
289 reduced carbon, which would drive metabolic processes in the cytoplasm and other cellular
290 compartments, such as the mitochondrion, while enabling the import of Pi into the chloroplast,
291 which sustains ATP synthesis.

292 **The *tpt3* mutant has reduced photosynthetic activity when grown in ML**

293 To understand the impact of the loss of CreTPT3 activity on PET, we quantified photosynthetic
294 activities following a transition from LL to ML (**Supplementary Fig. 5**). Photosynthetic O_2
295 evolution rates (OERs) were measured for WT, *t3ko2* and *C_T3KO2* over a range of light
296 intensities. LL acclimated WT, *t3ko2*, and *C_T3KO2* showed comparable OERs at intensities
297 below 200 μmol photons m^{-2} s^{-1}, while at saturating light intensities of ≥600 μmol photons m^{-2} s^{-1},
298 the OER of *t3ko2* was diminished slightly relative to the WT and the complemented strain (**Fig.**
299 **4A**). Upon acclimation of the cells to ML for 24 h, the *t3ko2* mutant consistently displayed lower
300 OERs than WT cells or *C_T3KO2* under all actinic light intensities used (**Fig. 4A**). Additionally,
301 while the Fv/Fm in the mutant grown in LL was comparable to that of WT and *C_T3KO2* (**Fig.**
302 **4B**), after exposure of the mutant cells to ML for 6 h, the Fv/Fm declined to about 50% of the WT
303 and *C_T3KO2* levels; the decline in the mutant continued over a period of 24 h in ML, with a 3-
304 fold decrease in Fv/Fm for *t3ko2* compared to that of WT cells (**Fig. 4B**). These results indicate
305 that damage to PSII reaction centers occurs following exposure of the mutant to ML.

306 To examine the redox state of the photosynthetic apparatus, the pool of electron acceptors
307 downstream of PSII were evaluated. We quantified the photochemical efficiency (qL) of all strains
308 at various light intensities after growth in LL or shifting them to ML for 6 and 24 h (**Fig. 4C**). The
309 photosynthetic parameter qL indicates the redox state of Q_A, the primary electron acceptor of the

310 PSII reaction center. Assuming that Q_A and Q_B are in equilibrium, qL would reflect the redox
311 status of the PQ pool; a lower qL value indicates a more reduced electron transport chain (Kramer
312 et al., 2004). 1-qL positively correlates with the PQ pool redox state. In the LL-acclimated cells,
313 1-qL was significantly higher in *t3ko2* even at low levels of actinic illumination compared to that
314 of WT cells and the rescued strain. For cells that had been acclimated to ML (6 h and 24 h), 1-qL
315 was 70% of the near maximum value for *t3ko2*, even under relatively low actinic light conditions
316 (e.g. 100 µmol photons m^{-2} s^{-1}), indicating a highly reduced PQ pool. In contrast, for WT and the
317 complemented strain at the same light intensity, the 1-qL value attained only ~20% of the
318 maximum value (**Fig. 4C**). These results suggest that the PQ pool is much more reduced in LL-
319 acclimated *t3ko2* relative to WT and *C_T3KO2* (**Fig. 4C**), and that there is a much more
320 pronounced reduction of this pool at all actinic light intensities in ML grown *t3ko2* mutants. These
321 results suggest a limitation in electron flow downstream of the PQ pool in both LL and ML grown
322 *t3ko2*.

323 Moreover, we analyzed how fast PET becomes restricted following the transfer of LL-grown *t3ko2*,
324 *C_T3KO2* and WT cells to HL (400-450 µmol photons m^{-2} s^{-1}) by monitoring changes in the redox
325 state of the PQ pool. We observed that the PQ pool in *t3ko2* began to be more reduced than that of
326 WT cells and *C_T3KO2* after 105 s of elevated illumination (**Fig. 4D**), and that this was even more
327 pronounced at longer times in HL. These results suggest that PET can be rapidly limited by
328 diminished triose-P export from the chloroplast; elimination of CreTPT3 has a strong impact on
329 PET activity.

330 To determine if PSI was also impacted in the mutant cells, we analyzed PSI/P700
331 oxidation/reduction kinetics following exposure of LL-grown cells to ML in the presence of
332 DCMU (20 µM) and hydroxylamine (1 mM) to block a contribution of electrons from PSII. Levels
333 of photo-oxidizable P700 following exposure to actinic light for 5 sec were similar in all LL-
334 acclimated strains (**Fig. 4E**). However, the level of photo-oxidized P700 in ML-acclimated cells
335 declined in the mutant to ~40-50% of that in WT and *C_T3KO2* cells (**Fig. 4E**), indicating that
336 PSI is more reduced in the *t3ko2* mutant after ML exposure. As shown in **Fig. 4F**, the oxidation
337 rate of P700 following a dark to light transition was much slower in the ML-acclimated *t3ko2*
338 compared to that of WT. These results suggest that the mutant has a diminished level of available
339 electron acceptors on the acceptor side of PSI (relative to WT and *C_T3KO2*) after growth in ML.

340 **CreTPT3 inactivation dramatically affected accumulation and distribution of**
341 **compartmentalized H_2O_2**

342 To investigate the relationship of CreTPT3 activity to oxidative stress, we assayed ROS production
343 in the mutant using the fluorescent probe CM-H2DCFDA, which upon exposure to increasing
344 ROS levels is converted to the green-fluorescent molecule dichlorofluorescein (DCF). DCF
345 fluorescence was visualized by confocal microscopy. As shown in **Fig. 5A** and **B**, ROS levels in
346 the *t3ko2* mutant were markedly increased (~3-fold) after 48 h in ML, while little difference in
347 ROS levels was detected in WT cells.

348 For an alternative, dynamic method for evaluating redox changes in the chloroplast, we used the
349 redox sensitive green fluorescent protein roGFP2, which was targeted to the chloroplast stroma
350 (**Fig. 5C**, upper panel) and mitochondrion (**Fig. 5C**, lower panel). roGFP2 monitors ratiometric
351 redox changes of glutathione, which reflects cellular ROS levels (Dorion et al., 2021; Vevea et al.,
352 2013). LL-acclimated WT cells and the *t3ko2* mutant exhibited similar levels of chloroplast
353 roGFP2 oxidation (**Fig. 5D**). Upon transfer of these cells to ML, the mutant showed an increase in
354 chloroplast oxidative conditions, with a 5.0-fold increase after 1.5 h, and a 2.0-fold increase after
355 6 h, which is 1.8- and 1.6-fold higher than the values measured in WT cells (**Fig. 5D**). Additionally,
356 as triose-P is exported to the cytosol by CreTPT3, it could potentially be further metabolized and
357 donate redox equivalents to the mitochondrial electron transport chain and alter mitochondrial
358 ROS production. Therefore, we also measured mitochondrial redox levels at different light
359 intensities in both WT and the *t3ko2* mutant using the roGFP2 sensor targeted to the mitochondrion.
360 Upon a LL to ML shift for 1.5 and 6.0 h, neither WT nor *t3ko2* displayed a significant change in
361 fluorescence from the mitochondrial targeted roGFP (**Fig. 5E**). These results suggest that the
362 mitochondrial redox level is maintained after shifting either LL acclimated WT or *t3ko2* cells to
363 ML. Overall, the inability to export triose-P through CreTPT3 markedly increased the level of
364 oxidative stress in the chloroplast but not in the mitochondrion.

365 We also determined if the ROS accumulated in *t3ko2* is H_2O_2 and whether this molecule shows
366 differential accumulation in the different subcellular compartments; the analysis was based on the
367 use of a hypersensitive sensor of H_2O_2, roGFP2-Tsa2ΔCR, which was previously used for studies
368 with Chlamydomonas (Niemeyer et al., 2021). In this analysis, we monitored real-time
369 accumulation of H_2O_2 in the stroma, cytosol, mitochondrion, and nucleus (**Fig. 6A**) following a 20

370 min exposure of the cells to either HL or very low light (**Fig. 6B-E**). The *t3ko2* stromal H_2O_2 level
371 increased within 2.5 min of the light exposure and attained a 1.4-fold increase after 20 min of
372 illumination with HL compared to the initial level in LL (**Fig. 6B**). The stromal H_2O_2 levels in WT
373 cells showed little change after being shifted to HL, however, the level declined when the cells
374 were shifted to 10 μmol photons m^{-2} s^{-1}, or very low light. Notably, after 20 min in HL, the stroma
375 of the *t3ko2* mutant accumulated ~1.6-fold more H_2O_2 than that of the WT cells; *t3ko2* mutant cells
376 in very low light accumulated a similar amount of stromal H_2O_2 as WT cells after exposure to HL
377 (**Fig. 6B**). The cytosolic probe also responded rapidly, with a 1.2-fold increase for WT and a 1.4-
378 fold increase for the *t3ko2* mutant (**Fig. 6C**); note that the initial levels of H_2O_2 prior to the transfer
379 of the cells to HL or very low light were much lower in the WT cells than in the mutant. The *t3ko2*
380 cytosolic H_2O_2 level was elevated relative to the level in WT cells by 2.1-fold after 20 min of
381 illumination in HL (**Fig. 6C**). We did not observe a significant change in H_2O_2 levels in the
382 mitochondrion for either the WT or the *t3ko2* mutant after the cells were shifted to the higher light
383 intensity (**Fig. 6D**). Finally, the *t3ko2* mutant already accumulated much higher levels of H_2O_2 in
384 the nucleus in LL compared to that in the WT cells, although both mutant and WT cells did not
385 show significant changes in nuclear H_2O_2 levels after HL exposure (**Fig. 6E**).

386

387 **Discussion**

388 **Cre*TPT2* and Cre*TPT3* genes exhibit different expression patterns**

389 In this study, we discovered that Chlamydomonas contains at least two TPTs that are located on
390 the chloroplast envelope. An earlier report suggested that CreTPT2 was a plastidic PPT (for the
391 transport of PEP) (Bockwoldt et al., 2019), but based on our results, it appears to be functionally
392 more similar to a triose-P transporter. In vitro assays show that CreTPT2 has almost the same
393 substrate specificity as CreTPT3, although it may be less effective in DHAP/Pi exchange (**Fig.**
394 **1C-E**). To determine expression patterns of Cre*TPT2* and Cre*TPT3*, the abundance of the Cre*TPT2*
395 and Cre*TPT3* transcripts were analyzed using RT-qPCR and by mining published RNA-seq data
396 over the diurnal cycle, and during nitrogen/sulfur/iron starvation (Zones et al., 2015; Ngan et al.,
397 2015; González-Ballester et al., 2010; Urzica et al., 2013) (**Supplementary Fig. 1C-D,** and **9**).
398 Cre*TPT3* was highly expressed in the light and dark, with significantly higher transcript
399 accumulation than that of Cre*TPT2* and the other genes (Cre*TPT10* and *CGL51*) potentially
400 encoding chloroplast localized pPTs (**Supplementary Fig. 1C-D**). Cre*TPT2* and Cre*TPT3* also
401 responded differentially to abiotic stresses. Cre*TPT3* was strongly induced by nitrogen, sulfur, and
402 iron starvation and upon exposure to HL, whereas the level of the Cre*TPT2* transcript remained
403 almost unchanged under the same conditions (**Supplementary Fig. 9A-D**), suggesting that
404 CreTPT3 plays a more prominent role in exporting triose-P from the chloroplast than CreTPT2,
405 with potentially increasing export from the plastid under HL and nutrient limitation conditions.
406 This hypothesis is supported by the observation that *tpt3* mutants displayed much more severe
407 growth retardation relative to *tpt2* mutants upon exposure to ML or HL (**Fig. 2C**). There is no
408 evidence showing that the *TPTs* from plants are induced by stress/excess absorbed excitation, and
409 expression of the Arabidopsis *TPT* gene appears to even decrease following HL exposure (Weise
410 et al., 2019).

411 Cre*TPT2* and Cre*TPT3* exhibited distinct expression patterns over the diurnal cycle; the expression
412 of Cre*TPT2* increased rapidly after transitioning from the dark to the light, with peak accumulation
413 after one hour in the light, when the transcript level of Cre*TPT3* was at its lowest (**Supplementary**
414 **Fig. 1D**). Continued exposure to light led to a decrease in the level of the Cre*TPT2* transcript to
415 near zero while the transcript from Cre*TPT3* steadily increased in the light, reaching a peak in mid-

416 day (**Supplementary Fig. 1D**). The Cre*TPT2* expression pattern suggests that it might play a role
417 in exporting triose-P at the beginning of light period, when the light intensity and photosynthesis
418 are low and low levels of triose-P would be synthesized in the stroma. As the light intensity
419 increases over the course of the day, higher levels of triose-P are synthesized and its trafficking
420 out of the chloroplast for use in other subcellular compartments would likely predominantly
421 involve the activity of CreTPT3. The greater specificity of CreTPT3 than CreTPT2 for transporting
422 DHAP (**Fig. 1E**) may make it more effective than CreTPT2 in transporting C3 phosphorylated
423 compounds. This possibility is congruent with the finding that there is elevated
424 synthesis/accumulation of CreTPT3 mRNA during the day when the light intensity reaches its
425 peak (Zones et al. 2015) and there would be rapid synthesis of the C3 phosphorylated compounds.
426 Overall, the subfunctionalization of the two Chlamydomonas triose-P transporters based on their
427 expression levels, patterns of RNA accumulation over the course of the day and upon nutrient
428 deprivation, and their substrate specificities, may help tune the export of triose-P from the
429 chloroplast with respect to the diurnal cycle and dynamic environmental cues.

430 **CreTPT3 also potentially serves as a redox valve, transferring reductant to the cytoplasm**

431 It was previously proposed that chloroplast TPTs could catalyze two potential reactions in the light
432 (**Fig. 7**) based on the crystal structure of the red algal TPT (Lee et al., 2017) and in vitro assays
433 using isolated spinach chloroplasts (Stocking and Larson, 1969); both triose-P/Pi, and triose-P/3-
434 PGA exchange across the chloroplast inner envelope membrane. The former reaction can route
435 both carbon skeletons and reductants into the cytoplasm while importing Pi back into the
436 chloroplast for ATP regeneration. The latter reaction would import 3-PGA into the chloroplast in
437 exchange for triose-P (DHAP, GAP), which would serve to transfer reductant from the chloroplast
438 to the cytosol while transferring 3-PGA back into the chloroplast where it can be reduced by the
439 CBBC and stimulate the regeneration of ribulose 1,5-bisphosphate. Indeed, in vitro, CreTPT3 can
440 actively transport both triose-P and 3-PGA in exchange for Pi (**Fig. 1**), indicating that this
441 transporter can serve as both a carbon and 'reductant shuttle' which would help sustain
442 photosynthetic electron flow.

443 Studies of photosynthetic activities and growth of WT and *tpt3* mutants (e.g. *t3ko2*) in LL, ML
444 and HL support the idea that the mutant is highly compromised in its ability to export fixed carbon
445 and potentially also reductant from the chloroplast. In *t3ko2* exposed to LL (after growth in LL),

446 growth was slow (**Fig. 2E**) and the PQ pool (**Fig. 4C**) was more reduced than in WT cells, while
447 there was little loss of PSII or PSI activities (**Fig. 4A, B, E, F**). These results suggest that there is
448 a reduced rate of PQH2 oxidation. During ML exposure, the mutant stopped growing, and when
449 placed in HL experienced severe bleaching (**Fig. 2F**). The highly reduced PQ pool and PSI reaction
450 center in ML-acclimated *t3ko2* cells (**Fig. 4C, E**, respectively) reflects hyper reduction of PET and
451 the generation of 'over-flow' electrons. The phenotypes of the *t3ko2* cells, including an elevated
452 1-qL (**Fig. 4C-D**), slower oxidation rate of PSI in ML-acclimated cells (**Fig. 4F**), accumulation of
453 storage carbon (**Fig. 3A-D**), an increase in intracellular accumulation of triose-P and 3-PGA (**Fig.**
454 **3E**), light dependent damage to the photosynthetic apparatus (**Fig. 4B**) and elevated
455 production/accumulation of ROS (**Fig. 5A, B**), especially in the chloroplast (**Fig. 6B**), indicates a
456 block on the acceptor side of PSI, which reflects the function of CreTPT3 and its central role in
457 fixed carbon export from the chloroplast and for fueling central metabolism. Furthermore, the
458 inability to efficiently transport fixed carbon from the chloroplast in ML and HL would result in
459 diminished CBBC activity, diminished photosynthetic electron transport and the hyper-reduction
460 of the stroma, which would also result in diminished ATP synthesis and NADPH production.

461 The malate-OAA shuttle represents another route that, under high redox stress, might have
462 partially compensated for the loss of the CreTPT3 by transporting reductant from the chloroplast
463 (schematic in **Fig. 7**). Intriguingly, malate levels in *t3ko2* were 4-fold lower than in WT cells (**Fig.**
464 **3E**, **G**). Moreover, expression of the plastid localized malate dehydrogenases (Cre*MDH1* and
465 Cre*MDH5*) was 3-fold to 5-fold lower in the mutant than in WT cells following a transition from
466 LL to ML (**Supplementary Fig. 10D-E**), indicating that the malate-OAA shuttle is likely unable
467 to compensate for a loss of CreTPT3. Inactivation of CreTPT3 appears to have a negative impact
468 on the malate-OAA shuttle, potentially because of the compromised physiological state of the
469 *t3ko2* mutant. Furthermore, a previous study of metabolic flux analysis during heterotrophic
470 growth of Chlamydomonas showed that the CreTPT shuttle(s) is almost 10-fold more active than
471 the malate-OAA shuttle (Boyle et al., 2017).

472 **TPT deficiency in Chlamydomonas cannot be compensated for by a day/night regime**

473 TPT deficiency in plants can be almost fully compensated for by the starch-mediated night
474 pathways that elicit the breakdown of starch and the export of the breakdown products via the
475 maltose transporter (MEX1) and glucose translocator (GlcT) (Niittylä et al., 2004; Cho et al., 2011).

476 Furthermore, in plants, starch turnover may also be occurring in the light, at the same time as starch
477 is being synthesized (Häusler et al., 1998; Walters et al., 2004). Compared to algae, plant cells
478 appear to display a high plasticity in their capacity to transport fixed carbon between the
479 chloroplast and cytosol. This high degree of plasticity in plants is reflected by the findings: i) most
480 dicots contain a larger number of pPTs (from 5 to 16) (Bockwoldt et al., 2019). For example,
481 Arabidopsis contains 6 pPTs, which includes one TPT, two GPTs, two PPTs and one XPT
482 (Bockwoldt et al., 2019), whereas Chlamydomonas harbors four pPTs, which include two TPTs,
483 one putative PPT (TPT10 in this study) and one putative GPT/XPT (CGL51 in this study); ii) the
484 plant TPTs play an important role in the export of carbon from the chloroplast during the day.
485 However, XPT has been shown to transport triose-Ps and partially compensate for the loss of TPTs
486 under both ML and HL conditions (Eicks et al., 2002; Hilgers et al., 2018b). Hence, it appears that
487 the paths for fixed carbon export in plants are cooperative, with contributions of transporters that
488 use various sugars, sugar phosphates and triose phosphates.

489 Additionally, the elevated starch content in the *t3ko2* mutant during growth in both LL and ML
490 compared to WT cells suggests that the lesion creates a bottleneck in the export of fixed carbon,
491 which in part becomes stored as starch and lipids (**Fig. 3A-D, Supplementary Fig. 8A**). The
492 conversion of triose-P to starch releases Pi within the chloroplast that can at least partially
493 compensate for the shortage of Pi caused by inactivation of CreTPT3 (Börnke and Sonnewald,
494 2011). Thus, photosynthetic carbon assimilation can be maintained until the cellular system is
495 completely compromised. In this study, we found that Chlamydomonas *tpt3* mutants exhibited
496 severe growth retardation and the accumulation of starch and lipid in either continuous light (CL)
497 or when experiencing a day/night regime (**Fig. 2D-G** and **8A**). Furthermore, the light-induced
498 electron transport rate (ETR) through PSII in the *t3ko2* mutant maintained on a diurnal cycle was
499 similar to that of WT cells exposed to actinic light intensities of up to 200 μmol photons m^{-2} s^{-1},
500 but was approximately 30% lower than that of WT cells at a light intensity of 400 μmol photons
501 m^{-2} s^{-1} (**Fig. 8B**). We also observed that diurnally maintained *t3ko2* cells grew slightly better than
502 when the cells were maintained in CL (**Fig. 8A**), indicating that the loss of CreTPT3 might be
503 partially compensated for by starch turnover during the night (or allow for some repair of cellular
504 damage that might accumulate during the day), but to a lesser extent than in plants. We observed
505 night-time starch degradation in *tpt3* cells, although immediately following the night period a
506 higher level (~5-fold) of undegraded starch remained relative to that of WT cultures (**Fig. 8C**).

507 These data suggest that starch mobilization may partially compensate for a CreTPT3 deficiency in
508 Chlamydomonas.

509 The mechanism by which starch breakdown products are exported from the chloroplast during the
510 night in Chlamydomonas remains largely unknown, although it could involve various transporters
511 including MEX1 (like in plants). Chlamydomonas MEX1 can transport starch break down
512 products in the form of glucose and/or glucose phosphate, but there is no evidence suggesting that
513 it can export maltose since a *mex1* mutant did not accumulate maltose or exhibit growth
514 impairment (Findinier et al., 2017). We speculate that the loss of TPT3 might be partially
515 compensated for by starch turnover in the dark, with degradation products exported via MEX1 or
516 other pPTs that are highly expressed in the dark and downregulated in the light, such as CreTPT10
517 and CGL51 (**Supplementary Fig. 1D**). However, even if hexose-P is exported from the
518 chloroplast, it may not be readily converted to triose-P (see below), which would fuel the TCA
519 cycle and respiration and serve to support anabolic processes.

520 ***t3ko2* experiences oxidative stress**

521 In plants, the export of sugars and other molecules (e.g. redox equivalents, ROS) can serve as
522 signals that coordinate chloroplast and nuclear gene expression during acclimation to HL (Häusler
523 et al., 2014; Zirngibl et al., 2022). We probed the impact of impaired triose-P export in *t3ko2* on
524 ROS production and accumulation in various subcellular compartments following exposure of the
525 cells to ML or HL. In plant cells, H_2O_2 is produced as a side-product of cellular processes including
526 PET, mitochondrial respiration, and substrate level oxidation (Smirnoff and Arnaud, 2019; Foyer
527 and Noctor, 2016). While ROS stability is generally low, it can accumulate in cells experiencing
528 oxidative stress, with H_2O_2 being the most prevalent species that can function as a redox messenger
529 (Li and Kim, 2022). Moreover, the trafficking of H_2O_2 into or out of different cellular
530 compartments can trigger activation of other retrograde and anterograde signals that may
531 coordinate activities among the compartments, including the nucleus (Exposito-Rodriguez et al.,
532 2017; Mittler et al., 2022; Shapiguzov et al., 2012). Upon exposure to HL, the *t3ko2* mutant
533 accumulated more stromal H_2O_2 than WT cells. The cytosolic H_2O_2 levels in the mutant exhibited
534 a similar increase, which may reflect the ability of this metabolite to rapidly diffuse from the
535 chloroplast and into the cytoplasm (**Fig. 6B, C**). Furthermore, it is unlikely that the mitochondrion
536 contributes to an increase in H_2O_2 in *t3ko2* since no (or little) increase in accumulation of

537 intramitochondrial H_2O_2 was observed in the mutant in either LL or ML (**Fig. 6D**). An increase in
538 H_2O_2 accumulation in the nucleus of *t3ko2* relative to WT cells was also observed, although the
539 light intensity (HL or LL) did not alter these levels in either WT or the mutant (**Fig. 6E**); a previous
540 report showed that the nuclear H_2O_2 level was not significantly affected in WT Chlamydomonas
541 cells following a HL exposure (Niemeyer et al., 2021), which may reflect both the level of H_2O_2
542 accumulation and barriers that limit its diffusion. The higher levels of H_2O_2 in the nucleus of *t3ko2*
543 cells may trigger retrograde signals that modulate nuclear gene expressions, which in turn could
544 ameliorate some of the negative effects of ROS and elicit repair of any damage experienced by the
545 photosynthetic apparatus. A similar response may be elicited in WT cells at higher intensity actinic
546 light.

547 Superoxide is predominantly produced by PSI, which can enzymatically be converted into H_2O_2
548 (Foyer, 2018). Highly reduced PSI in the *tpt3* mutant can lead to an increase in the production of
549 H_2O_2. It was also shown that H_2O_2 can be synthesized in thylakoid membranes as a consequence
550 of the oxidation of plastoquinol (PQH_2), suggesting a positive correlation between the redox state
551 of the PQ pool and the generation of H_2O_2 (Khorobrykh et al., 2015). A similar finding was noted
552 for both *Nicotiana benthamiana* and Chlamydomonas based on the use of hypersensitive H_2O_2
553 sensors (Exposito-Rodriguez et al., 2017; Niemeyer et al., 2021). These two organisms were
554 shown to accumulate more stromal H_2O_2 in HL, which was dependent on photosynthesis. We
555 observed this positive correlation between PQ pool reduction and the accumulation of H_2O_2 in the
556 *t3ko2* mutant; the PQ pool was more reduced in *t3ko2* relative to the WT cells after exposing the
557 cells to 105 s of HL (**Fig. 4D)**. In parallel, there was a marked increase in stromal H_2O_2 following
558 2.5 min of HL (**Fig. 6B**). Therefore, hyper-reduction of the PQ pool in the mutant likely results in
559 elevated stromal H_2O_2 accumulation, suggesting that CreTPT3 activity and the export of triose-P
560 from the chloroplast is critical for maintaining low level synthesis/accumulation H_2O_2 and
561 sustaining a high rate of PET in HL; the export of fixed carbon relieves the redox pressure and
562 lessens ROS formation. Additionally, Cre*TPT3* is the most nutrient-deprivation
563 responsive/upregulated of the *pPT* family genes; it responds strongly to nitrogen, sulfur, and iron
564 deprivation (**Supplementary Fig. 9 B-D**). These findings are in accord with the hypothesis that
565 the ability to traffic fixed carbon from the chloroplast is important for both the distributing carbon
566 to other cellular compartments and relieving oxidative stress in the organelle.

567 **CreTPT3 is critical for maintaining intracellular partitioning of fixed carbon**

568 Why is the phenotype of the Chlamydomonas *tpt3* mutant so severe? Land plants contain the entire
569 glycolytic pathway in both the chloroplast and cytosol while the pathway is partitioned between
570 two compartments in Chlamydomonas; 90% of the upper activities of the pathways (from F6P→
571 3PG) was associated with the plastid while over 95% of the activities of the lower part of the
572 pathway (3PG→Pyruvate) occurred in the cytosol (Klein, 1986; Rochaix et al., 1998). The
573 oxidative pentose phosphate pathway also appears to be in the chloroplast (Klein, 1986). The
574 partitioning of glycolysis between the chloroplast and cytosol is supported by the comparative
575 quantification of the metabolites, with glucose-1-P, fructose-6-P, and fructose-1,6-P2 being
576 exclusively in the chloroplast and 2-phosphoglycerate only in the cytosol (Klöck and Kreuzberg,
577 1991). Recently, it was suggested that the flux of metabolites through hexose-P is negligible in the
578 Chlamydomonas cytosol (Treves et al., 2022), possibly because of the absence of glycolytic
579 reactions that would facilitate its metabolism. Therefore, even if hexose-P is exported from the
580 chloroplast, it would likely not be rapidly metabolized or maintain rapid cell growth. Overall, the
581 results strongly suggest that triose-P exported from the Chlamydomonas chloroplast is likely the
582 major source of fixed carbon transported into the cytoplasm of the cell, facilitating algal growth in
583 the light.

584 Thus, we hypothesize that the export of triose-P would drive the cytosolic segment of glycolysis
585 and downstream metabolic pathways. This hypothesis is supported by the metabolite analysis;
586 specifically, a marked increase of most metabolites associated with the upper-
587 glycolytic/gluconeogenic pathways, and a significant decrease of some metabolites of the TCA
588 cycle upon exposure of the mutant cells to either LL or ML (**Fig. 3E-G, Supplementary Fig. 8B,**
589 **C**). In contrast, elimination of the chloroplast-targeted TPT1 protein of Arabidopsis showed no
590 significant phenotype, although growth was retarded in the TPT/XPT double mutants (Hilgers et
591 al., 2018a). Furthermore, based on Pearson correlation analyses presented in **Supplementary Fig.**
592 **11** and **Table. 4**, Cre*TPT3* is co-expressed with many genes involved in respiratory electron
593 transport and the major ATP transporters located on the mitochondria and chloroplast envelope
594 membranes. In addition, transcript levels of some genes involved in starch degradation, glycolysis,
595 the TCA cycle, and malate/OAA shuttle shared a high correlation coefficient with Cre*TPT3*.
596 Together, these data indicate that the export of triose-P from the chloroplast is closely linked to

central energy metabolism in Chlamydomonas, starting with the production of triose-P in the chloroplast by the CBBC or starch degradation (chloroplast localized reactions of glycolysis), followed by transport to the cytosol which houses the remaining reactions of glycolysis. The products of glycolysis can be trafficked to the mitochondria where they can be used to drive the TCA cycle, respiratory metabolism, and the generation of ATPs (**Supplementary Fig. 11**). Hence, triose-P is the major photoassimilate routed from the chloroplast, supplying substrates for downstream metabolic processes.

Summary

As depicted in **Fig. 7**, we propose that various tiers of regulation are responsible for the physiological responses of the Chlamydomonas *t3ko2* mutant. When *t3ko2* cells are transferred from LL to ML, the triose-P pool and metabolites derived from that pool accumulate because of the reduced capacity of the strain to move triose-P out of the chloroplast where it could be further metabolized. Some compensation may occur through the activity of other transporters, although expression of Cre*TPT2* is especially low during the day (in the light) and the transport of hexose phosphate may not compensate for the loss of CreTPT3 because the cytoplasm does not have (or has little of) the activities of glycolysis that would convert hexose-P to DHAP. The compromised ability to export fixed carbon from the chloroplast also suppresses CBBC activity, causes hyper-reduction of PET and the accumulation of ROS (which would inhibit photosynthetic activity). The highly diminished export of triose-P to the cytoplasm would compromise respiration and downstream biosynthetic processes. Furthermore, hyper-reduction of PET and accumulation of carbon metabolites in the stroma would activate AGPase through allosteric regulation and by the FDX/TRX (ferredoxin/thioredoxin) and NTRC (NADPH-dependent thioredoxin reductase C) redox systems, which would result in starch hyper-accumulation (Ballicora et al., 2000; Lepistö et al., 2013) (**Fig. 7**). Increased ROS accumulation in the mutant chloroplasts and an elevated PET redox state would also elicit the generation of retrograde signals that mediate changes in nuclear gene expression (Wakao and Niyogi, 2021; Suzuki et al., 2012; Shapiguzov et al., 2012), stimulating the synthesis of specific activities that may function to ameliorate the impact of the hyper-reduced state attained in the chloroplast.

626 **Material and methods**

627 **Strains and culture conditions**

628 WT Chlamydomonas M10 (CC-4403, isogenic line derived from CC-124) was used as the parental
629 strain for the generation of knockout mutants. Cultures were routinely cultivated in growth
630 chambers (LED-41L2, Percival Scientific, Inc.) at 25°C with continuous shaking on an orbital
631 shaker (VWR OS-500 Shaker) at 120 rpm, in Tris-Acetate-Phosphate (TAP) medium (Harris,
632 2009). Cultures were illuminated with continuous cool white LEDs (LED-41L2, Percival
633 Scientific, Inc.) at low light (LL, 30 µmol photons m^{-2} s^{-1}). Experiments were mostly performed
634 with cells grown in the photoautotrophic TP medium (TAP medium without acetate) and in some
635 cases, in TAP medium, at 25ºC, and sparged with air while being shaken at 120 rpm in a growth
636 chamber (LED-41L2, Percival Scientific, Inc.). For growth assays, cultures were inoculated to a
637 density of 0.02 at $OD_{750\ nm}$ (~1×10^5 cells/mL) in TP sparged with air under either LL or moderate
638 light (ML, 250-300 µmol photons m^{-2} s^{-1}) intensities. For spectrophotometric and chlorophyll
639 fluorescence analyses, the experimental design is described in **Supplementary Fig. 5**. Growth
640 assays on solid medium were performed with cultures spotted onto the medium at different
641 dilutions (indicated in the text) and exposed to different light intensities; spot tests for
642 photoautotrophic growth were on TP agar plates and for mixotrophic growth on TAP agar plates.
643 Agar plates were incubated for 7 d under either LL or ML (cool white LED) at 25°C.

644 **Reconstitution into liposomes and transport assays**

645 The procedures for the construction and expression of Cre*TPT2* and Cre*TPT3* in yeast are
646 described in supplemental information (SI). For uptake studies, yeast membranes from cells with
647 and without recombinant His-tagged CreTPT2 or CreTPT3 were enriched and reconstituted into
648 3% (w/v) L-alpha-phosphatidylcholine using a freeze-thaw-sonication procedure (Linka et al.,
649 2008). The reconstituted liposomes were preloaded with 30 mM Pi or phosphorylated metabolites
650 to be tested as potential transport substrates. As a negative control for antiport activity, liposomes
651 were also generated without metabolite preloading. The external counter-exchange substrate was
652 removed via gel filtration on Sephadex G-25M columns (GE Healthcare). Transport assays were
653 initiated by adding 0.25 mM [alpha-^{32}P]-phosphoric acid (6,000 Ci/mmol) to the medium bathing
654 the liposomes and performed as previously described by Linka et al. (2008). Measurements of Km
655 for Pi and competitive inhibition constants (Ki) are described in supplemental information (SI).

656 **Vector construction, transformation, and subcellular localization**

657 The pRam118_VENUS plasmid, which harbors the VENUS gene and the *AphVII* cassette (confers
658 resistance to hygromycin) (Cre01.g045550)(Kaye et al., 2019), was used to express Cre*TPT2*
659 (Cre06.g263850_4532) and Cre*TPT3* (Cre01.g045550_4532). The step-by-step description is in
660 SI. 2-4 µg of the engineered plasmids was linearized and added to 250 µL of a cell suspension of
661 ~3×10^8 cells/mL per reaction. The GeneArt MAX Efficiency Transformation Reagent for algae
662 (Invitrogen) was used for introducing the plasmid into the algal cells by electroporation according
663 to the instructions provided by the manufacturer. Transformants were selected on solid TAP
664 medium containing hygromycin (10 µg/mL; Enzo Life).

665 Drug resistant transformants were visualized for VENUS fluorescence as previously described
666 (Kaye et al., 2019). In brief, transgenic cell lines resistant to hygromycin were screened for
667 VENUS fluorescence using a microplate reader (Infinite M1000; TECAN). Excitation and
668 emission settings were: VENUS, excitation at 515 nm, bandwidth 12 nm and emission at 550 nm,
669 bandwidth 12 nm; chlorophyll excitation was at 440 nm, bandwidth 9 nm and emission was at 680
670 nm, bandwidth 20 nm. The TCS SP8 confocal laser-scanning microscope (Leica) was used to
671 visualize the VENUS fluorescence signal (Kaye et al., 2019).

672 **CRISPR-CAS9 mediated mutagenesis**

673 The Chlamydomonas WT strain CC-124 was used for mutant generation. WT cells were cultured
674 under CL (50 µmol photons m^{-2} s^{-1}) for 2 d to a density of 3-5×10^6 cells/mL. The cells were then
675 concentrated to 2×10^8 cells/mL in 0.5×TAP medium supplemented with 80 mM sucrose. Two
676 single guide RNAs (sgRNA) were designed by CHOPCHOP and synthesized by Integrated DNA
677 Technologies (IDT). The sequences of the generated sgRNAs are: *TPT2*-sg (5′-
678 AUAAGGGCAAGGACAUGUCAGGG -3) for editing exon 8, *TPT3*-sg1 (5′-
679 CGCUGGGCGTCACUUCCCGGCGG -3′) for editing exon 1, and *TPT3*-sg2 (5′-
680 AAGGCCGCUAUCGCCAACGUGGG -3′) for editing of exon 7. The protocol for disruption of
681 Cre*TPT2* and Cre*TPT3* was adapted from (Findinier et al., 2019) and is described in SI.

682 **Complementation of mutants *tpt3* mutants**

683 Mutant strains were transformed with the linearized pRam118_CreTPT3 plasmid. Transformed
684 cells were selected in ML and screened for VENUS fluorescence. Colonies exhibiting VENUS

685 fluorescence and an *AphVII* cassette knock-in at the CAS9 target site were examined for
686 accumulation of the CreTPT3 protein by immunodetection using CreTPT3 antibodies generated
687 by GenScript USA Inc (Piscataway, USA). Immuno-positive colonies were subjected to growth
688 assays using spot tests under ML on either solid TAP or TP medium.

689 **P700 activity measurements**

690 Absorbance spectroscopy [JTS-100 spectrophotometer (SpectroLogiX, TN)] to measure P700
691 activity was performed with dark-adapted liquid cultures (15 µg/mL chlorophyll, in 20 mM
692 HEPES-KOH, pH 7.2, and 10% ficoll) as previously described (Clowez et al., 2021). Actinic light
693 was provided by an orange LED (165 µmol photons m^{-2} s^{-1}) for PSI oxidation, followed by a
694 saturating pulse and dark incubation. 20 µM DCMU and 1 mM hydroxylamine were added to the
695 cell suspension to inhibit linear electron flow (LEF) prior to the measurement. P700 activity was
696 measured by monitoring the absorbance at 705 nm (interference filter 6 nm FWHM was used to
697 create a narrow excitation beam); the absorbance at 740 nm was used to correct for an unspecific
698 contribution to the 705 nm signal.

699 **Chlorophyll fluorescence analysis**

700 Chlorophyll fluorescence used to evaluate photosynthetic electron transport was monitored with a
701 DUAL PAM-100 fluorometer. Cells were acclimated in the dark for 20 min prior to illumination
702 at increasing light intensities (0, 10, 50, 100, 200, 400, 800, 1000, 1200 µmol photons m^{-2} s^{-1}) for
703 2 min at each intensity, or at a constant intensity of 450 µmol photons m^{-2} s^{-1} for 10 min to evaluate
704 1-qL. 1 mM CO_2 ($NaHCO_3$) was added to the reaction mix as an electron acceptor for the CBBC.

705 **ROS measurements and roGFP2 imaging analysis**

706 All strains were grown photoautotrophically in LL for 16-24 h. After dilution with fresh medium,
707 the cultures were transferred to ML and stained with CM-H2DCFDA (Thermo Fisher Scientific)
708 as described in (Kong et al., 2018) for detecting ROS. A step-by-step protocol is given in SI.

709 Constructs containing chloroplast or mitochondria targeting sequences (Crozet et al., 2018) fused
710 to codon-optimized roGFP2 (Vevea et al., 2013) were transformed into WT and mutant strains.
711 Transgenic cell lines were screened for green roGFP2 fluorescence using a microplate reader
712 (Infinite M1000; TECAN); excitation was at 488 nm, bandwidth 9 nm and emission at 525 nm,

713 bandwidth 10 nm. Cells with strong green fluorescence were cultured as depicted in
714 **Supplementary Fig. 5**. Signals from the transformed lines were visualized using a TCS SP8
715 confocal laser-scanning microscope (Leica). roGFP2 signals were collected and analyzed as
716 previously described (Vevea et al., 2013). Using the sequential setup of the SP8, roGFP2 signals
717 were collected at the emission wavelength of 510-550 nm immediately following excitation at 405
718 nm and 488 nm (Vevea et al., 2013). The degree of roGFP2 oxidation was analyzed as the ratio of
719 the emission signals after excitation at 405 nm and 488 nm (Vevea et al., 2013).

720 Plasmids harboring H_2O_2 roGFP2-Tsa2ΔCR sensors (Niemeyer et al., 2021) were obtained from
721 the Chlamydomonas Resource Center (https://www.chlamycollection.org/) (**Supplementary**
722 **Table. 3)**. Cells in which roGFP2-Tsa2ΔCR was targeted to the stroma, cytosol, mitochondrial
723 matrix, or nucleus were initially grown in LL in TAP to exponential growth phase. Cells were then
724 grown in TP in LL for 2 h and shifted either to HL or very low light (10 µmol photons m^{-2} s^{-1}).
725 Prior to collecting the algal samples, N-Ethylmaleimide (NEM) (in 100-mM MES–Tris buffer, pH
726 7.0) was added to a centrifuge tube to trap the oxidation state of the sensor. The final concentration
727 of NEM is 10 mM after adding the algae culture. After centrifugation (1459 x g, 3 min), cells were
728 resuspended in 100-mM MES–Tris buffer (pH 7.0) to reach the chlorophyll concentration of 30
729 µg/mL; and roGFP2 fluorescence was measured in a plate reader (Infinite M1000; TECAN). For
730 calibration and data calculation, fully oxidized sensors in the control samples were prepared by
731 adding H_2O_2 to a final concentration of 5 mM, and fully reduced sensors were prepared by adding
732 DTT to a final concentration of 100 mM. Signals were detected using the excitation wavelengths
733 of 410 and 488 nm and the emission wavelength of 514 nm. The degree of sensor oxidation (OxD)
734 was calculated using the previous equation as described in (Niemeyer et al., 2021).

735 **Photosynthesis-Irradiance curve**

736 Photosynthesis-Irradiance curves were measured using a custom Pt-Ag/AgCl polarographic
737 electrode system (ALGI) with a water jacketed (for temperature-control), 1 mL glass reaction
738 chamber. A step-by-step protocol is provided in SI.

739 **Starch and TAG quantification**

740 Cells were grown under LL to mid-exponential phase, diluted to 0.5 µg/mL chl with fresh medium
741 and transferred to and then grown in ML for 24 h or more, as indicated. Starch was measured

742 according to (Klein and Betz, 1978), with slight modification (see SI). Triacylglycerol (TAG)
743 levels were estimated by a fluorometric assay using the dye Nile Red (Thermo Fisher)(Yu et al.,
744 2009). A Nile Red solution (500 µg/mL in acetone) was added to 1 mL of the cell suspensions to
745 a final concentration of 0.5 µg/mL. Samples were then incubated at room temperature for 30 min,
746 and the Nile Red fluorescence emission quantified at 575 nm following excitation at 530 nm using
747 a microplate reader (Infinite M1000; TECAN).

748 **Metabolic analysis**

749 Cells grown in LL were shifted to ML for 45 min or 6 h, as indicated. 45 mL of culture was rapidly
750 quenched in cold saline solution (-2 to -3°C), extracted using cold methanol and then analyzed by
751 LC-MS/MS. Quenching and analysis of metabolites were performed, with modifications,
752 according to (Sake et al., 2020). A step-by-step protocol is described in SI. Metabolite extracts
753 were analyzed using LC-MS/MS, as adapted from (Young et al., 2011). A Phenomenex 150 mm
754 x 2 mm Synergi Hydro-RP column was used on an Agilent 1200 Series HPLC system coupled to
755 an AB Sciex 5500 QTRAP system. LC was performed with a liquid injection volume of 20 µL and
756 a gradient elution with 10 mM tributylamine and 15 mM acetic acid (aqueous phase) in acetonitrile
757 (organic phase) (reagent B) at a constant flow rate of 0.3 mL/min, and a constant temperature of
758 40°C. The gradient profile of the organic phase is as follows: 0% B (0 min), 8% B (10 min), 16%
759 B (15 min), 30% B (16.5 min), 30% B (19 min), 90% B (21.5 min), 90% B (28 min), 0% B (28.5
760 min), and 0% B (35 min). MS analysis was performed in negative mode using a multiple reaction
761 monitoring (MRM) acquisition method. Data acquisition was performed on the ABSciex Analyst
762 1.7 software. Absolute quantification of intracellular metabolites was performed using the
763 quantitation mode on the Analyst software. All chemicals used for metabolite extraction and LC-
764 MS/MS analysis were Optima grade reagents.

765

Acknowledgments:

WH thanks Dr. Masayuki Onishi for advice on the generation of CRISPR mutants and Adrien Burlacot for help with PQ pool measurements.

Funding:

This project has supported by DOE award DE-SC0019417 to ARG. WH was supported solely by a grant from the US Department of Energy, Office of Science, Basic Energy Systems (DE-SC0019417). AK and MCP were supported solely by a grant from the US Department of Energy, Office of Science, Basic Energy Systems (DE-SC0019341 to MP). NB and MM were supported by US Department of Energy, Office of Science, Office of Biological and Environmental Research (BER), (DE-SC0018301 to NB). NL and AP were supported by German Research Foundations (DFG Grant LI1781/2-2). BR was supported by National Science Foundation (Award Number 1645164). RGK and JF were supported by the Department of Plant Biology of the Carnegie Institution for Science. PR was supported by Human Frontier Science Program (HFSP) RGP0046/2018 (to ARG).

Author contributions:

WH, AK, ARG and MP conceptualized the study. WH generated the CRISPR mutants as well as the complemented strain, localized the TPT2 and 3 proteins, analyzed the photosynthetic performances and starch changes over diel cycle. AK performed the experiments of photosynthetic O_2 evolution, extraction of samples for LC-MS/MS, data analysis of LC-MS/MS. AP and NL performed the reconstitution into liposomes and transport activity assays. MM and NB performed LC-MS/MS and analyses of metabolite data. WH and YW analyzed the redox status in the cell. BR performed data mining for transcriptome and the Nile red staining. JF and NF analyzed starch changes upon transition from LL to ML. WH, PR and ARG analyzed PSI and PSII activities. JF and BR constructed roGFP2 associated vectors. WH and ARG wrote the manuscript. ARG, MP, AK, NL, NB, AP, MM and all the other authors helped writing and revising the manuscript.

Competing interests:

All authors declare they have no competing interests.

Distribution of materials:

All manuscripts must include the following statement as an unnumbered footnote: "The author(s) responsible for distribution of materials integral to the findings presented in this article in accordance with the policy described in the Instructions for Authors (https://academic.oup.com/plcell/pages/General-Instructions) are: Weichao Huang (whuang@carnegiescience.edu) and Arthur Grossman (agrossman@carnegiescience.edu).

800 **References**

801 **Badger, M.R., von Caemmerer, S., Ruuska, S., and Nakano, H.** (2000). Electron flow to
802 oxygen in higher plants and algae: rates and control of direct photoreduction (Mehler
803 reaction) and rubisco oxygenase. Philos. Trans. R. Soc. Lond. B Biol. Sci. **355**: 1433–1446.

804 **Ballicora, M.A., Frueauf, J.B., Fu, Y., Schürmann, P., and Preiss, J.** (2000). Activation of the
805 potato tuber ADP-glucose pyrophosphorylase by thioredoxin. J. Biol. Chem. **275**: 1315–
806 1320.

807 **Bhatt, P., Bhandari, G., Turco, R.F., Aminikhoei, Z., Bhatt, K., and Simsek, H.** (2022). Algae
808 in wastewater treatment, mechanism, and application of biomass for production of value-
809 added product. Environ. Pollut. **309**: 119688.

810 **Bockwoldt, M., Heiland, I., and Fischer, K.** (2019). The evolution of the plastid phosphate
811 translocator family. Planta **250**: 245–261.

812 **Börnke, F. and Sonnewald, S.** (2011). Biosynthesis and metabolism of starch and sugars. In Plant
813 Metabolism and Biotechnology (John Wiley & Sons, Ltd: Chichester, UK), pp. 1–25.

814 **Boyle, N.R., Sengupta, N., and Morgan, J.A.** (2017). Metabolic flux analysis of heterotrophic
815 growth in *Chlamydomonas reinhardtii*. PLoS One **12**: e0177292.

816 **Chaux, F., Burlacot, A., Mekhalfi, M., Auroy, P., Blangy, S., Richaud, P., and Peltier, G.**
817 (2017). Flavodiiron proteins promote fast and transient O_2 photoreduction in
818 Chlamydomonas. Plant Physiol. **174**: 1825–1836.

819 **Cho, M.-H., Lim, H., Shin, D.H., Jeon, J.-S., Bhoo, S.H., Park, Y.-I., and Hahn, T.-R.** (2011).
820 Role of the plastidic glucose translocator in the export of starch degradation products from
821 the chloroplasts in *Arabidopsis thaliana*. New Phytol. **190**: 101–112.

822 **Clowez, S., Renicke, C., Pringle, J.R., and Grossman, A.R.** (2021). Impact of menthol on
823 growth and photosynthetic function of *Breviolum minutum* (Dinoflagellata, Dinophyceae,
824 Symbiodiniaceae) and Interactions with its Aiptasia Host. J. Phycol. **57**: 245–257.

825 **Crozet, P. et al.** (2018). Birth of a photosynthetic chassis: A MoClo toolkit enabling synthetic
826 biology in the microalga *Chlamydomonas reinhardtii*. ACS Synth. Biol. **7**: 2074–2086.

827 **Dorion, S., Ouellet, J.C., and Rivoal, J.** (2021). Glutathione metabolism in plants under stress:
828 beyond reactive oxygen species detoxification. Metabolites **11**: 641.

829 **Eicks, M., Maurino, V., Knappe, S., Flügge, U.-I., and Fischer, K.** (2002). The plastidic pentose
830 phosphate translocator represents a link between the cytosolic and the plastidic pentose
831 phosphate pathways in plants. Plant Physiol. **128**: 512–522.

832 **Exposito-Rodriguez, M., Laissue, P.P., Yvon-Durocher, G., Smirnoff, N., and Mullineaux,**
833 **P.M.** (2017). Photosynthesis-dependent H_2O_2 transfer from chloroplasts to nuclei provides
834 a high-light signalling mechanism. Nat. Commun. **8**: 49.

835 **Findinier, J., Delevoye, C., and Cohen, M.M.** (2019). The dynamin-like protein Fzl promotes
836 thylakoid fusion and resistance to light stress in *Chlamydomonas reinhardtii*. PLoS Genet.
837 **15**: e1008047.

838 **Fischer, K., Kammerer, B., Gutensohn, M., Arbinger, B., Weber, A., Hausler, R.E., and**
839 **Flugge, U.-I.** (1997). A new class of plastidic phosphate translocators: A putative link
840 between primary and secondary metabolism by the phosphoenolpyruvate/phosphate
841 antiporter. Plant Cell **9**: 453.

842 **Fliege, R., Flügge, U.-I., Werdan, K., and Heldt, H.W.** (1978). Specific transport of inorganic
843 phosphate, 3-phosphoglycerate and triosephosphates across the inner membrane of the
844 envelope in spinach chloroplasts. Biochim. Biophys. Acta Bioenerg. **502**: 232–247.

845 **Flügge, U.I., Fischer, K., Gross, A., Sebald, W., Lottspeich, F., and Eckerskorn, C.** (1989).
846 The triose phosphate-3-phosphoglycerate-phosphate translocator from spinach
847 chloroplasts: nucleotide sequence of a full-length cDNA clone and import of the in vitro
848 synthesized precursor protein into chloroplasts. EMBO J. **8**: 39–46.

849 **Flügge, U.I., Häusler, R.E., Ludewig, F., and Fischer, K.** (2003). Functional genomics of
850 phosphate antiport systems of plastids. Physiol. Plant. **118**: 475–482.

851 **Foyer, C.H.** (2018). Reactive oxygen species, oxidative signaling and the regulation of
852 photosynthesis. Environ. Exp. Bot. **154**: 134–142.

853 **Foyer, C.H. and Noctor, G.** (2016). Stress-triggered redox signalling: what's in pROSpect? Plant
854 Cell Environ. **39**: 951–964.

855 **Ge, F., Huang, W., Chen, Z., Zhang, C., Xiong, Q., Bowler, C., Yang, J., Xu, J., and Hu, H.**
856 (2014). Methylcrotonyl-CoA carboxylase regulates triacylglycerol accumulation in the
857 model diatom *Phaeodactylum tricornutum*. Plant Cell **26**: 1681–1697.

858 **Gibson, D.G., Young, L., Chuang, R.-Y., Venter, J.C., Hutchison, C.A., 3rd, and Smith, H.O.**
859 (2009). Enzymatic assembly of DNA molecules up to several hundred kilobases. Nat.
860 Methods **6**: 343–345.

861 **Gietz, R.D. and Schiestl, R.H.** (2007). High-efficiency yeast transformation using the LiAc/SS
862 carrier DNA/PEG method. Nat. Protoc. **2**: 31–34.

863 **González-Ballester, D., Casero, D., Cokus, S., Pellegrini, M., Merchant, S.S., and Grossman,**
864 **A.R.** (2010). RNA-seq analysis of sulfur-deprived Chlamydomonas cells reveals aspects
865 of acclimation critical for cell survival. Plant Cell **22**: 2058–2084.

866 **Harris, E.H.** (2009). Chlamydomonas sourcebook: Introduction to Chlamydomonas and its
867 laboratory use 2nd ed. (Academic Press).

868 **Häusler, R.E., Baur, B., Scharte, J., Teichmann, T., Eicks, M., Fischer, K.L., Flügge, U.I.,**
869 **Schubert, S., Weber, A., and Fischer, K.** (2000). Plastidic metabolite transporters and

870 their physiological functions in the inducible crassulacean acid metabolism plant
871 Mesembryanthemum crystallinum. Plant J. **24**: 285–296.

872 **Häusler, R.E., Heinrichs, L., Schmitz, J., and Flügge, U.-I.** (2014). How sugars might
873 coordinate chloroplast and nuclear gene expression during acclimation to high light
874 intensities. Mol. Plant **7**: 1121–1137.

875 **Häusler, R.E., Schlieben, N.H., Schulz, B., and Flügge, U.I.** (1998). Compensation of decreased
876 triose phosphate/phosphate translocator activity by accelerated starch turnover and glucose
877 transport in transgenic tobacco. Planta **204**: 366–376.

878 **Helman, Y., Tchernov, D., Reinhold, L., Shibata, M., Ogawa, T., Schwarz, R., Ohad, I., and**
879 **Kaplan, A.** (2003). Genes encoding A-type flavoproteins are essential for photoreduction
880 of O2 in cyanobacteria. Curr. Biol. **13**: 230–235.

881 **Hilgers, E.J.A., Schöttler, M.A., Mettler-Altmann, T., Krueger, S., Dörmann, P., Eicks, M.,**
882 **Flügge, U.-I., and Häusler, R.E.** (2018a). The combined loss of triose phosphate and
883 xylulose 5-Phosphate/Phosphate translocators leads to severe growth retardation and
884 impaired photosynthesis in *Arabidopsis thaliana* tpt/xpt double mutants. Front. Plant Sci.
885 **9**: 1331.

886 **Hilgers, E.J.A., Staehr, P., Flügge, U.-I., and Häusler, R.E.** (2018b). The Xylulose 5-
887 Phosphate/Phosphate Translocator Supports Triose Phosphate, but Not
888 Phosphoenolpyruvate Transport Across the Inner Envelope Membrane of Plastids in
889 Arabidopsis thaliana Mutant Plants. Front. Plant Sci. **9**: 1461.

890 **Houille-Vernes, L., Rappaport, F., Wollman, F.-A., Alric, J., and Johnson, X.** (2011). Plastid
891 terminal oxidase 2 (PTOX2) is the major oxidase involved in chlororespiration in
892 Chlamydomonas. Proc. Natl. Acad. Sci. U. S. A. **108**: 20820–20825.

893 **Huang, W., Haferkamp, I., Lepetit, B., Molchanova, M., Hou, S., Jeblick, W., Río Bártulos,**
894 **C., and Kroth, P.G.** (2018). Reduced vacuolar β-1,3-glucan synthesis affects carbohydrate
895 metabolism as well as plastid homeostasis and structure in *Phaeodactylum tricornutum*.
896 Proc. Natl. Acad. Sci. U. S. A. **115**: 4791–4796.

897 **Jack, D.L., Yang, N.M., and Saier, M.H., Jr** (2001). The drug/metabolite transporter superfamily.
898 Eur. J. Biochem. **268**: 3620–3639.

899 **Johnson, X. and Alric, J.** (2013). Central carbon metabolism and electron transport in
900 Chlamydomonas reinhardtii: metabolic constraints for carbon partitioning between oil and
901 starch. Eukaryot. Cell **12**: 776–793.

902 **Kammerer, B., Fischer, K., Hilpert, B., Schubert, S., Gutensohn, M., Weber, A., and Flügge,**
903 **U.I.** (1998). Molecular characterization of a carbon transporter in plastids from
904 heterotrophic tissues: the glucose 6-phosphate/phosphate antiporter. Plant Cell **10**: 105–
905 117.

906 **Kaye, Y., Huang, W., Clowez, S., Saroussi, S., Idoine, A., Sanz-Luque, E., and Grossman,**
907 **A.R.** (2019). The mitochondrial alternative oxidase from *Chlamydomonas reinhardtii*
908 enables survival in high light. J. Biol. Chem. **294**: 1380–1395.

909 **Khan, M.I., Shin, J.H., and Kim, J.D.** (2018). The promising future of microalgae: current status,
910 challenges, and optimization of a sustainable and renewable industry for biofuels, feed, and
911 other products. Microb. Cell Fact. **17**: 36.

912 **Khorobrykh, S.A., Karonen, M., and Tyystjärvi, E.** (2015). Experimental evidence suggesting
913 that H_2O_2 is produced within the thylakoid membrane in a reaction between plastoquinol
914 and singlet oxygen. FEBS Lett. **589**: 779–786.

915 **Klein, U.** (1986). Compartmentation of glycolysis and of the oxidative pentose-phosphate pathway
916 in *Chlamydomonas reinhardii*. Planta **167**: 81–86.

917 **Klein, U. and Betz, A.** (1978). Fermentative metabolism of hydrogen-evolving *Chlamydomonas*
918 *moewusii*. Plant Physiol. **61**: 953–956.

919 **Klöck, G. and Kreuzberg, K.** (1991). Compartmented metabolite pools in protoplasts from the
920 green alga *Chlamydomonas reinhardtii*: changes after transition from aerobiosis to
921 anaerobiosis in the dark. Biochim. Biophys. Acta **1073**: 410–415.

922 **Knappe, S., Flügge, U.-I., and Fischer, K.** (2003). Analysis of the plastidic phosphate
923 translocator gene family in Arabidopsis and identification of new phosphate translocator-
924 homologous transporters, classified by their putative substrate-binding site. Plant Physiol.
925 **131**: 1178–1190.

926 **Kong, F., Burlacot, A., Liang, Y., Légeret, B., Alseekh, S., Brotman, Y., Fernie, A.R.,**
927 **Krieger-Liszkay, A., Beisson, F., Peltier, G., and Li-Beisson, Y.** (2018). Interorganelle
928 communication: peroxisomal MALATE DEHYDROGENASE2 connects lipid catabolism
929 to photosynthesis through redox coupling in Chlamydomonas. Plant Cell **30**: 1824–1847.

930 **Kramer, D.M., Johnson, G., Kiirats, O., and Edwards, G.E.** (2004). New fluorescence
931 parameters for the determination of QA redox state and excitation energy fluxes.
932 Photosynth. Res. **79**: 209.

933 **Krishnan, A., Kumaraswamy, G.K., Vinyard, D.J., Gu, H., Ananyev, G., Posewitz, M.C., and**
934 **Dismukes, G.C.** (2015). Metabolic and photosynthetic consequences of blocking starch
935 biosynthesis in the green alga *Chlamydomonas reinhardtii sta6* mutant. Plant J. **81**: 947–
936 960.

937 **Lee, S.-K., Eom, J.-S., Voll, L.M., Prasch, C.M., Park, Y.-I., Hahn, T.-R., Ha, S.-H., An, G.,**
938 **and Jeon, J.-S.** (2014). Analysis of a triose phosphate/phosphate translocator-deficient
939 mutant reveals a limited capacity for starch synthesis in rice leaves. Mol. Plant **7**: 1705–
940 1708.

941 **Lee, Y., Nishizawa, T., Takemoto, M., Kumazaki, K., Yamashita, K., Hirata, K., Minoda, A.,**
942 **Nagatoishi, S., Tsumoto, K., Ishitani, R., and Nureki, O.** (2017). Structure of the triose-

943 phosphate/phosphate translocator reveals the basis of substrate specificity. Nat Plants **3**:
944 825–832.

945 **Lepistö, A., Pakula, E., Toivola, J., Krieger-Liszkay, A., Vignols, F., and Rintamäki, E.**
946 (2013). Deletion of chloroplast NADPH-dependent thioredoxin reductase results in
947 inability to regulate starch synthesis and causes stunted growth under short-day
948 photoperiods. J. Exp. Bot. **64**: 3843–3854.

949 **Li, M. and Kim, C.** (2022). Chloroplast ROS and stress signaling. Plant Commun **3**: 100264.

950 **Lim, L., Linka, M., Mullin, K.A., Weber, A.P.M., and McFadden, G.I.** (2010). The carbon and
951 energy sources of the non-photosynthetic plastid in the malaria parasite. FEBS Lett. **584**:
952 549–554.

953 **Linka, M., Jamai, A., and Weber, A.P.M.** (2008). Functional characterization of the plastidic
954 phosphate translocator gene family from the thermo-acidophilic red alga *Galdieria*
955 *sulphuraria* reveals specific adaptations of primary carbon partitioning in green plants and
956 red algae. Plant Physiol. **148**: 1487–1496.

957 **Loddenkötter, B., Kammerer, B., Fischer, K., and Flügge, U.I.** (1993). Expression of the
958 functional mature chloroplast triose phosphate translocator in yeast internal membranes
959 and purification of the histidine-tagged protein by a single metal-affinity chromatography
960 step. Proc. Natl. Acad. Sci. U. S. A. **90**: 2155–2159.

961 **Mittler, R., Zandalinas, S.I., Fichman, Y., and Van Breusegem, F.** (2022). Reactive oxygen
962 species signalling in plant stress responses. Nat. Rev. Mol. Cell Biol. **23**: 663–679.

963 **Moog, D., Nozawa, A., Tozawa, Y., and Kamikawa, R.** (2020). Substrate specificity of plastid
964 phosphate transporters in a non-photosynthetic diatom and its implication in evolution of
965 red alga-derived complex plastids. Sci. Rep. **10**: 1167.

966 **Ngan, C.Y. et al.** (2015). Lineage-specific chromatin signatures reveal a regulator of lipid
967 metabolism in microalgae. Nat Plants **1**: 15107.

968 **Niemeyer, J., Scheuring, D., Oestreicher, J., Morgan, B., and Schroda, M.** (2021). Real-time
969 monitoring of subcellular H_2O_2 distribution in *Chlamydomonas reinhardtii*. Plant Cell **33**:
970 2935–2949.

971 **Niittylä, T., Messerli, G., Trevisan, M., Chen, J., Smith, A.M., and Zeeman, S.C.** (2004). A
972 previously unknown maltose transporter essential for starch degradation in leaves. Science
973 **303**: 87–89.

974 **Niyogi, K.K. and Truong, T.B.** (2013). Evolution of flexible non-photochemical quenching
975 mechanisms that regulate light harvesting in oxygenic photosynthesis. Curr. Opin. Plant
976 Biol. **16**: 307–314.

977 **Prabhakar, V. et al.** (2010). Phosphoenolpyruvate provision to plastids is essential for
978 gametophyte and sporophyte development in Arabidopsis thaliana. Plant Cell **22**: 2594–
979 2617.

980 **Raghavendra, A.S. and Padmasree, K.** (2003). Beneficial interactions of mitochondrial
981 metabolism with photosynthetic carbon assimilation. Trends Plant Sci. **8**: 546–553.

982 **Riesmeier, J.W., Flügge, U.I., Schulz, B., Heineke, D., Heldt, H.W., Willmitzer, L., and**
983 **Frommer, W.B.** (1993). Antisense repression of the chloroplast triose phosphate
984 translocator affects carbon partitioning in transgenic potato plants. Proc. Natl. Acad. Sci.
985 U. S. A. **90**: 6160–6164.

986 **Rochaix, J.-D., Goldschmidt-Clermont, M., and Merchant, S.** (1998). The molecular biology
987 of chloroplasts and mitochondria in Chlamydomonas J.-D. Rochaix, M. Goldschmidt-
988 Clermont, and S. Merchant, eds (Plenum Publishing Corporation).

989 **Sake, C.L., Newman, D.M., and Boyle, N.R.** (2020). Evaluation of quenching methods for
990 metabolite recovery in photoautotrophic *Synechococcus sp*. PCC 7002. Biotechnol. Prog.
991 **36**: e3015.

992 **Saroussi, S., Sanz-Luque, E., Kim, R.G., and Grossman, A.R.** (2017). Nutrient scavenging and
993 energy management: acclimation responses in nitrogen and sulfur deprived
994 Chlamydomonas. Curr. Opin. Plant Biol. **39**: 114–122.

995 **Schneider, A., Häusler, R.E., Kolukisaoglu, Ü., Kunze, R., Van der Graaff, E., Schwacke, R.,**
996 **Catoni, E., Desimone, M., and Flügge, U.I.** (2002). An Arabidopsis thaliana knock-out
997 mutant of the chloroplast triose phosphate/phosphate translocator is severely compromised
998 only when starch synthesis, but not starch mobilisation is abolished. Plant Journal.

999 **Shapiguzov, A., Vainonen, J.P., Wrzaczek, M., and Kangasjärvi, J.** (2012). ROS-talk - how
1000 the apoplast, the chloroplast, and the nucleus get the message through. Front. Plant Sci. **3**:
1001 292.

1002 **Smirnoff, N. and Arnaud, D.** (2019). Hydrogen peroxide metabolism and functions in plants.
1003 New Phytol. **221**: 1197–1214.

1004 **Stocking, C.R. and Larson, S.** (1969). A chloroplast cytoplasmic shuttle and the reduction of
1005 extraplastid NAD. Biochem. Biophys. Res. Commun. **37**: 278–282.

1006 **Streatfield, S.J., Weber, A., Kinsman, E.A., Hausler, R.E., Li, J., Post-Beittenmiller, D.,**
1007 **Kaiser, W.M., Pyke, K.A., Flugge, U.-I., and Chory, J.** (1999). The
1008 phosphoenolpyruvate/phosphate translocator is required for phenolic metabolism, palisade
1009 cell development, and Plastid-dependent nuclear gene expression. Plant Cell **11**: 1609.

1010 **Strenkert, D., Schmollinger, S., Gallaher, S.D., Salomé, P.A., Purvine, S.O., Nicora, C.D.,**
1011 **Mettler-Altmann, T., Soubeyrand, E., Weber, A.P.M., Lipton, M.S., Basset, G.J., and**
1012 **Merchant, S.S.** (2019). Multiomics resolution of molecular events during a day in the life
1013 of Chlamydomonas. Proc. Natl. Acad. Sci. U. S. A. **116**: 2374–2383.

1014 **Suzuki, N., Koussevitzky, S., Mittler, R., and Miller, G.** (2012). ROS and redox signalling in
1015 the response of plants to abiotic stress. Plant Cell Environ. **35**: 259–270.

1016 **Treves, H., Küken, A., Arrivault, S., Ishihara, H., Hoppe, I., Erban, A., Höhne, M., Moraes,**
1017 **T.A., Kopka, J., Szymanski, J., Nikoloski, Z., and Stitt, M.** (2022). Carbon flux through
1018 photosynthesis and central carbon metabolism show distinct patterns between algae, C3
1019 and C4 plants. Nat Plants **8**: 78–91.

1020 **Urzica, E.I., Vieler, A., Hong-Hermesdorf, A., Page, M.D., Casero, D., Gallaher, S.D., Kropat,**
1021 **J., Pellegrini, M., Benning, C., and Merchant, S.S.** (2013). Remodeling of membrane
1022 lipids in iron-starved Chlamydomonas. J. Biol. Chem. **288**: 30246–30258.

1023 **Vevea, J.D., Alessi Wolken, D.M., Swayne, T.C., White, A.B., and Pon, L.A.** (2013).
1024 Ratiometric biosensors that measure mitochondrial redox state and ATP in living yeast
1025 cells. J. Vis. Exp.: 50633.

1026 **Wakao, S. and Niyogi, K.K.** (2021). Chlamydomonas as a model for reactive oxygen species
1027 signaling and thiol redox regulation in the green lineage. Plant Physiol. **187**: 687–698.

1028 **Walters, R.G., Ibrahim, D.G., Horton, P., and Kruger, N.J.** (2004). A mutant of Arabidopsis
1029 lacking the triose-phosphate/phosphate translocator reveals metabolic regulation of starch
1030 breakdown in the light. Plant Physiol. **135**: 891–906.

1031 **Weber, A.P.M., Linka, M., and Bhattacharya, D.** (2006). Single, ancient origin of a plastid
1032 metabolite translocator family in Plantae from an endomembrane-derived ancestor.
1033 Eukaryot. Cell **5**: 609–612.

1034 **Weise, S.E., Liu, T., Childs, K.L., Preiser, A.L., Katulski, H.M., Perrin-Porzondek, C., and**
1035 **Sharkey, T.D.** (2019). Transcriptional regulation of the glucose-6-phosphate/phosphate
1036 translocator 2 is related to carbon exchange across the chloroplast envelope. Front. Plant
1037 Sci. **10**: 827.

1038 **Winder, C.L., Dunn, W.B., Schuler, S., Broadhurst, D., Jarvis, R., Stephens, G.M., and**
1039 **Goodacre, R.** (2008). Global metabolic profiling of Escherichia coli cultures: an
1040 evaluation of methods for quenching and extraction of intracellular metabolites. Anal.
1041 Chem. **80**: 2939–2948.

1042 **Young, J.D., Shastri, A.A., Stephanopoulos, G., and Morgan, J.A.** (2011). Mapping
1043 photoautotrophic metabolism with isotopically nonstationary $^{(13)}$C flux analysis. Metab.
1044 Eng. **13**: 656–665.

1045 **Yu, E.T., Zendejas, F.J., Lane, P.D., Gaucher, S., Simmons, B.A., and Lane, T.W.** (2009).
1046 Triacylglycerol accumulation and profiling in the model diatoms *Thalassiosira*
1047 *pseudonana* and *Phaeodactylum tricornutum* (Baccilariophyceae) during starvation. J.
1048 Appl. Phycol. **21**: 669–681.

1049 **Zhao, Y. et al.** (2018). Malate transported from chloroplast to mitochondrion triggers production
1050 of ROS and PCD in *Arabidopsis thaliana*. Cell Res. **28**: 448–461.

1051 **Zhao, Y., Yu, H., Zhou, J.-M., Smith, S.M., and Li, J.** (2020). Malate circulation: linking
1052 chloroplast metabolism to mitochondrial ROS. Trends Plant Sci. **25**: 446–454.

1053 **Zirngibl, M.-E., Araguirang, G.E., Kitashova, A., Jahnke, K., Rolka, T., Kühn, C., Nägele,**
1054 **T., and Richter, A.S.** (2022). Triose phosphate export from chloroplasts and cellular sugar
1055 content regulate anthocyanin biosynthesis during high light acclimation. Plant Commun:
1056 100423.

1057 **Zones, J.M., Blaby, I.K., Merchant, S.S., and Umen, J.G.** (2015). High-Resolution Profiling of
1058 a Synchronized Diurnal Transcriptome from *Chlamydomonas reinhardtii* Reveals
1059 Continuous Cell and Metabolic Differentiation. Plant Cell **27**: 2743–2769.

1060

1061 **Figures**

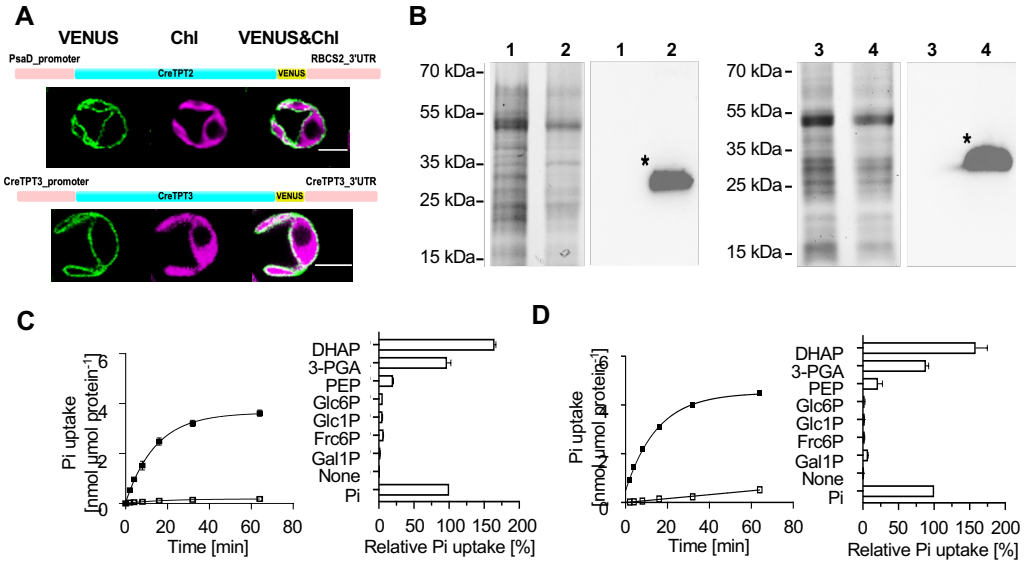

E

	Substrate	CreTPT2	CreTPT3
K_M	Pi	0,77 ± 0,05 mM	1.1 ± 0.2 mM
K_i	DHAP	0,71 ± 0,12 mM	0.57 ± 0.013 mM
K_i	3-PGA	0,78 ± 0,19 mM	0.79 ± 0.122 mM
K_i	PEP	Nd	Nd

Fig. 1: Subcellular localization of CreTPT2 and 3 and in vitro measurements of transport activities. (**A**) Cellular localization of CreTPT2 (upper) and CreTPT3 (lower). The construct for expression of the CreTPT2/3-VENUS fusion protein is shown above the cell images and described in the **Materials and methods**. VENUS fluorescence, green; Chlorophyll (Chl) autofluorescence, magenta. (Scale bar: 5 µm). (**B**) Expression of Cre*TPT2* (1, 2) and Cre*TPT3* (3, 4) in yeast. **Left in each panel**, SDS-PAGE of proteins from total membranes isolated from yeast cells containing the empty vector (1, 3) or expressing His-CreTPT2 (2) or His-CreTPT3 (4). **Right in each panel**, corresponding immunoblot blot detection of recombinant His-CreTPT2 or His-CreTPT3 protein using anti-His antibodies. The calculated molecular masses of the N-terminal His-tagged proteins of CreTPT2 and CreTPT3 were 39, and 37 kDa. (**C**) **Left**, kinetics of Pi exchange by His-CreTPT2 in lipid vesicles. Uptake of Pi (0.25 mM) into liposomes was measured in the presence (■) or absence (□) of Pi (30 mM) loaded into the vesicles. **Right**, analyses of substrate specificity of His-CreTPT2. (**D**) **Left**, kinetics of Pi exchange by His-CreTPT3 in lipid vesicles. Uptake of Pi (0.25 mM) into liposomes was measured in the presence (■) or absence (□) of Pi (30 mM) loaded into the vesicles. **Right**, analyses of substrate specificity of His-CreTPT3. For the left panels of **C** and **D**, the arithmetic mean (±SD) of three independent experiments (each with three technical replicates) was plotted with respect to the time after initiating the assay. For the right panels of **C** and **D**, liposomes in which His-CreTPT2 and His-CreTPT3, respectively, were incorporated, were preloaded with various substrates (30 mM) and the initial Pi uptake rates (at 0.25 mM external concentration) were determined. Relative velocities were compared to the Pi/Pi homo-exchange, which was set to 100%. The data represents the arithmetic mean (±SD) of three independent experiments (each consisting of three technical replicates). (**E**) Comparison of kinetic constants of His-CreTPT2 and His-CreTPT3. The Michaelis-Menten constant (K_M) for Pi uptake was determined using various external Pi concentrations (0.05-5 mM). The competitive inhibition constant (K_i) of Pi uptake (0.25 mM) was measured with increasing competitor concentrations (0.05-5 mM). Liposomes were preloaded with 30 mM Pi as the counter-exchange substrate. The data represent the arithmetic mean +/- SE of three independent experiments. Nd, no competitive inhibitory constant could be measured under the given experimental conditions. DHAP, dihydroxyacetone phosphate; 3-PGA, 3-phosphoglycerate; PEP, phosphoenolpyruvate; Glc6P, glucose 6-P; Glc1P, glucose 1-P; Fru6P, fructose 6-P; Gal1P, galactose 1-P.

1062

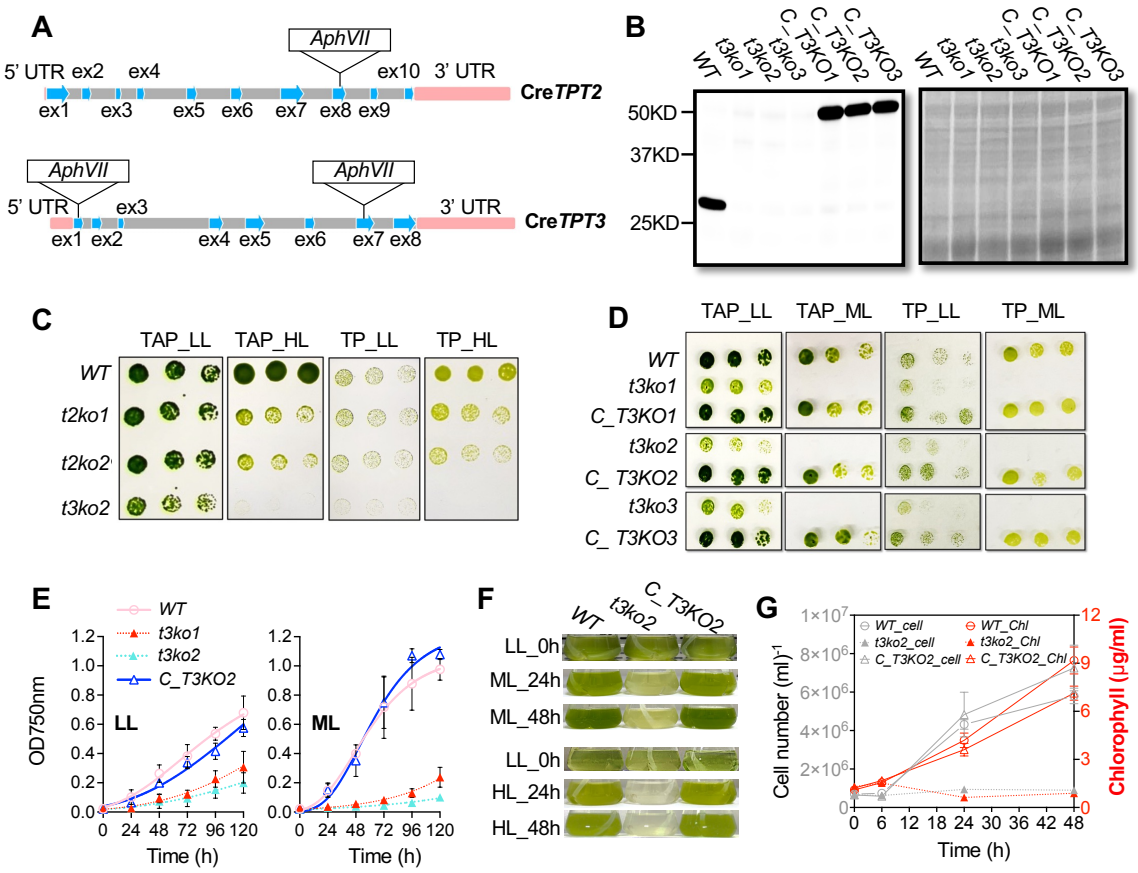

Fig. 2: Growth characterization of *tpt* mutants and complemented strains. (**A**) Molecular map of the Cre*TPT2* (upper) and Cre*TPT3* (lower) genes and the positions of the Cas9 targeted sites. Edited site of Cre*TPT2* is located in exon 8, edited sites of Cre*TPT3* are located in exons 1 and 7; *t3ko1* has the marker gene inserted in exon 1 and *t3ko2* and *t3ko3* have the marker gene inserted in exon 7. (**B**) Immunoblot (left panel) of the stained protein profiles (right panel) for wild type (WT), *t3ko1*, *t3ko2*, *t3ko3* and the complemented strains (*C_T3KO1*, *C_T3KO2* and *C_T3KO3*, respectively). (**C**) Growth of WT, *t2ko1*, *t2ko2*, and *t3ko2* at various dilutions (see below) on agar plates incubated under LL and HL for 4 d. (**D**) Growth of WT, *t3ko1*, *t3ko2*, *t3ko3* and the complemented strains (*C_T3KO1*, *C_T3KO2*, and *C_T3KO3*, respectively), at various dilutions (see below) on agar plates incubated under LL and ML for 4 d. (**E**) Growth of the various strains (indicated) in liquid medium under LL (left panel) and ML (right panel). (**F**) Transition of the strains from LL to ML (upper panel) or to HL (lower panel) for the times indicated. (**G**) Cell growth (number) and chlorophyll content of cultures at various times after shifting from LL to ML for up to 48 h. In **C** and **D**, the cells were spotted on agar plates containing TAP or TP medium and maintained under continuous LL, ML or HL conditions. The dilution series used was 1.5, 0.75, 0.375 μg/mL chlorophyll (left to right). For growth in liquid medium, the cells were cultured in TP medium to an initial OD_{750nm} 0.02 in air and under continuous LL before initiating the various growth analyses in LL, ML or HL. Each curve represents the arithmetic mean (±SD) of three independent experiments.

1063

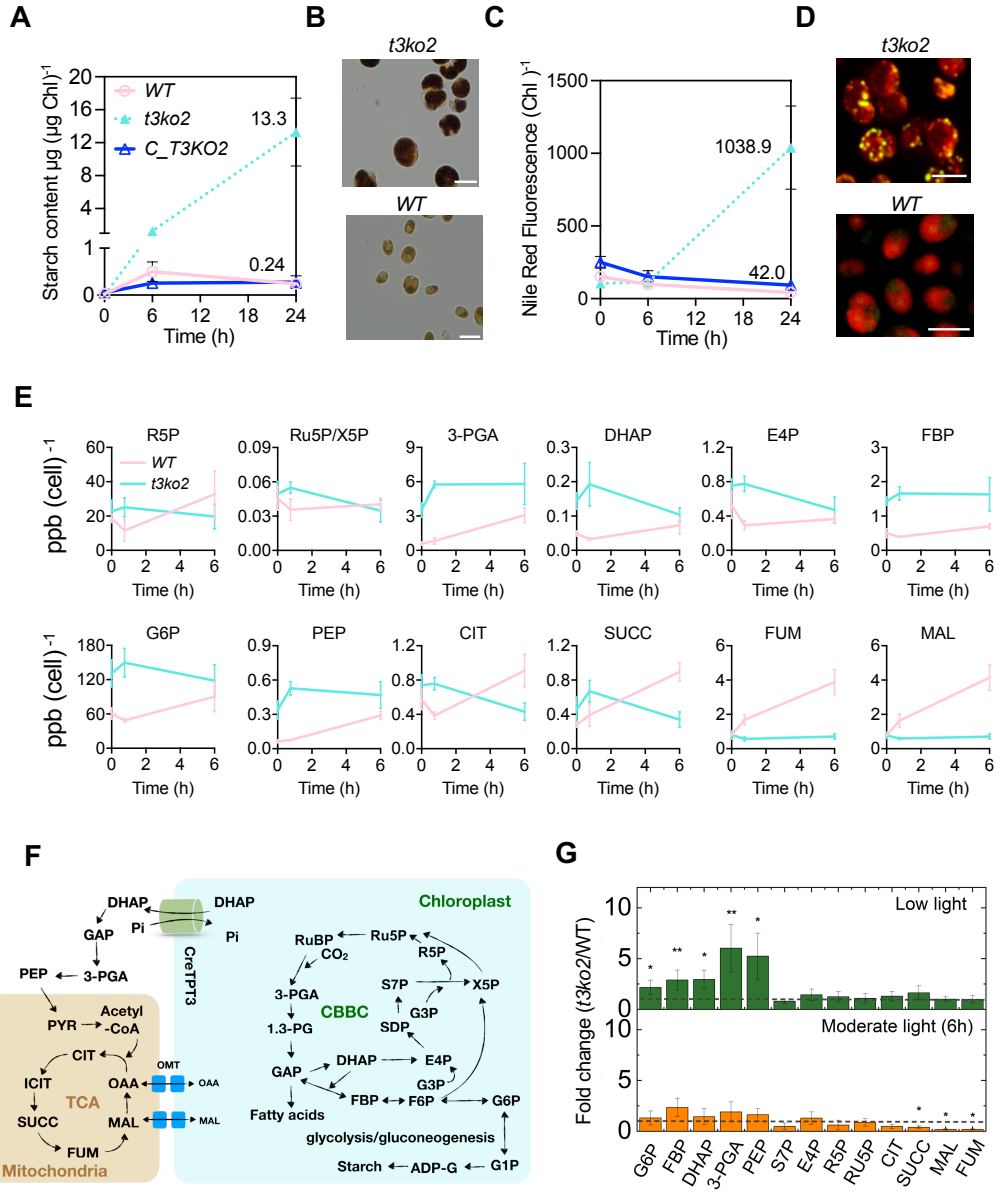

Fig. 3: Changes in storage carbon and metabolite levels in WT and *t3ko2* after transitioning cells from growth in LL to ML. (**A**) Starch content in indicated strains following 0, 6, and 24 h of ML exposure. (**B**) Lugol staining of starch in WT and *t3ko2* after 48 h of ML. (**C**) TAG (TAG: triacylglycerol) content in the indicated strains following 0, 6, and 24 h of ML exposure. (**D**) Nile Red staining of TAG in WT and *t3ko2* following 48 h of ML exposure. (**E**) Time course of metabolite accumulation at 0 h (LL), 45 min and 6 h following ML exposure. Data was normalized to cell numbers. Each data point shows the mean and standard error; the data represents three biological replicates for each metabolite. ppb: parts per billion. (**F**) Select metabolic pathways in Chlamydomonas adapted from (Johnson and Alric, 2013). (**G**) Bar graph representation of fold-change for metabolites shown in (**E**); calculated by dividing the mean of pool size in *t3ko2* by that of WT at the respective light levels. A fold change of 1 (no change) is indicated with a dashed line. An asterisk indicates statistically significant difference in pool sizes in *t3ko2* compared to WT (from **E**) (* P<0.05, ** P<0.01, *** P<0.001). Abbreviations: G6P, glucose-6-P; FBP, fructose bisphosphate; DHAP, dihydroxyacetone phosphate; 3-PGA, 3-phosphoglycerate; PEP, phosphoenolpyruvate; PYR, pyruvate; CIT, citrate; SUCC, succinate; FUM, fumarate; MAL, malate; E4P, Erythrose 4-P; R5P, Ribose 5-P; RU5P/X5P, ribulose 5-P/xylulose-5-P; OMT, 2-oxoglutarate/malate transporter.

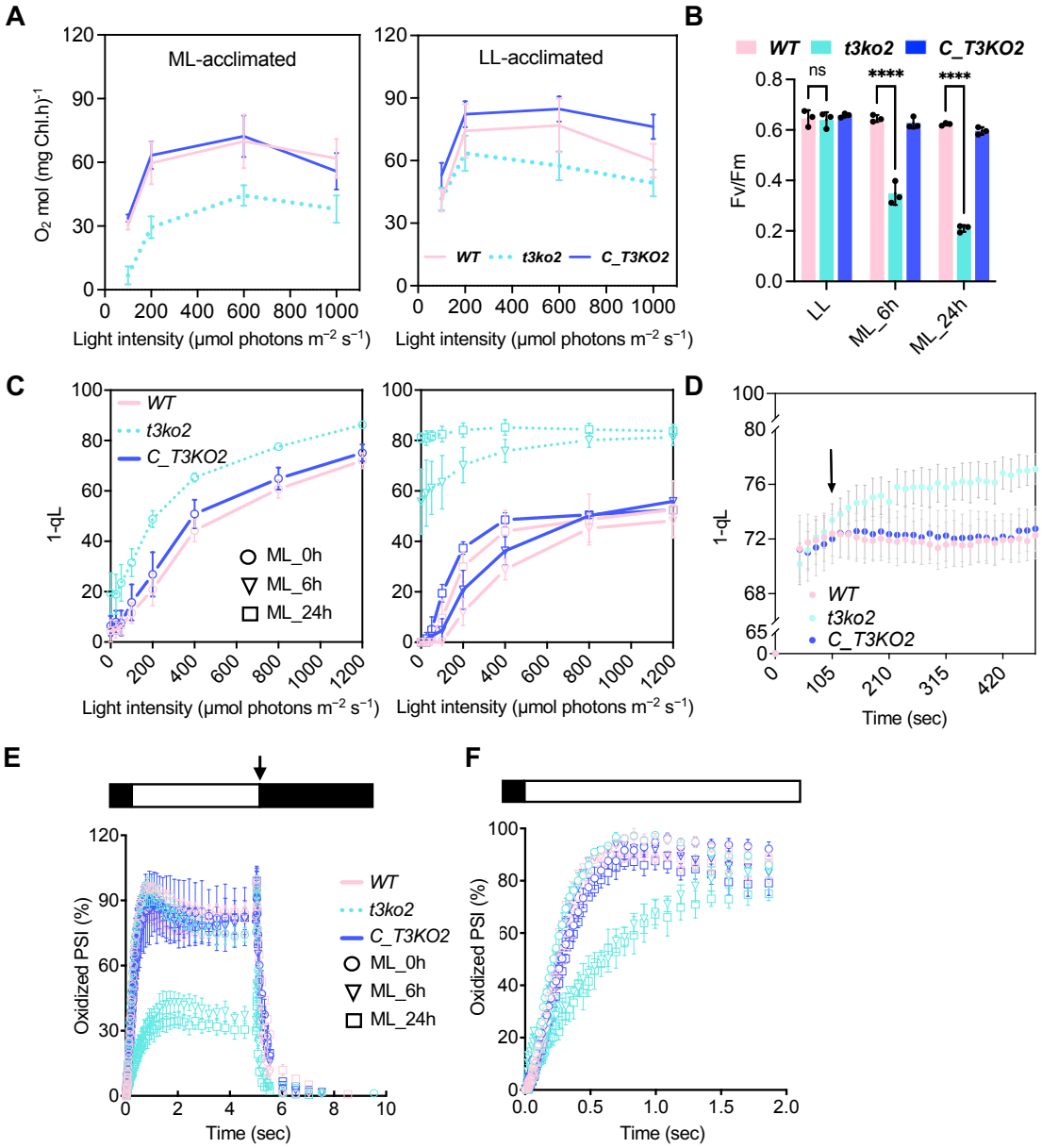

Fig. 4: Photosynthetic activities following a transition from LL to ML or to HL. (**A**) Light intensity curve of O_2 evolution of LL (left) and ML (right)-acclimated cells for the indicated strains. (**B**) Fv/Fm of WT, *t3ko2* and the rescued strain (*C_T3KO2*) following 0 (LL), 6 and 24 h in ML. (**C**) 1-qL values of LL (left panel) and ML (right panel) acclimated cells exposed to increasing actinic light intensities. (**D**) Kinetics of 1-qL of LL-acclimated cells after illumination at HL (400-450 µmol photons m^{-2} s^{-1}) for the times indicated on the x-axis. (**E**) P700 oxidation and reduction kinetics in LL-grown cells and after 6 and 24 h in ML. (**F**) Kinetics of P700 oxidation upon dark-to-light transition. P700 measurements were performed in the presence of DCMU and hydroxylamine, as indicated in the **Materials and methods**. Absorbance differences were monitored at 705 nm during continuous illumination with 150 µmol photons·m^{-2} s^{-1} for 5 sec (white box above), followed by a saturating light pulse at 1,500 µmol photons·m^{-2} s^{-1} (arrow) and a 5 sec dark incubation (black box). For panel **E**, the kinetics was normalized by setting maximum oxidation (after light pulse) of WT to 100% and for panel **F**, by setting maximum oxidation (after light pulse) of individual strain to 100%. The data from all panels represent the arithmetic mean (±SD) of three independent experiments. For panel **B**, the asterisks represent significant differences determined by ANOVA tests., ****P < 0.0001.

1065

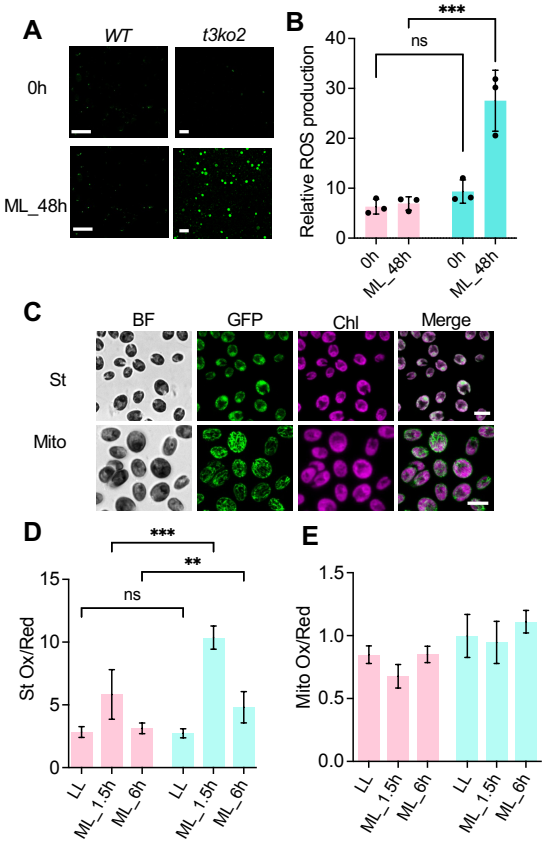

Fig. 5: Measurement of intracellular ROS in *t3ko2* and WT upon transition from LL to ML. (**A**) ROS levels were evaluated by CM-H2DCFDA fluorescence of WT and the *t3ko2* mutant in LL and following exposure to ML for 48 h. Scale bar: 20 μm. (**B**) Quantitation of data in **A**. Shown are mean values from three independent experiments, error bars represent standard deviation. roGFP2 protein was targeted to the chloroplast stroma (**C**, upper panel) and mitochondrion (**C**, lower panel). Scale bar: 10 μm; BF: bright field; roGFP2 fluorescence: green; Chlorophyll (Chl) autofluorescence: red. (**D-E**) Monitoring redox levels in stroma (**D**) and mitochondrion (**E**) after exposure of WT and the *t3ko2* mutant for 1.5 and 6.0 h of ML. Shown are mean values from three independent experiments, 3-4 random figures were analyzed for each experiment, error bars represent standard deviation. For panel **B** and **D**, the asterisks represent significant differences determined by ANOVA tests., **P < 0.005, ***P < 0.001.

1066

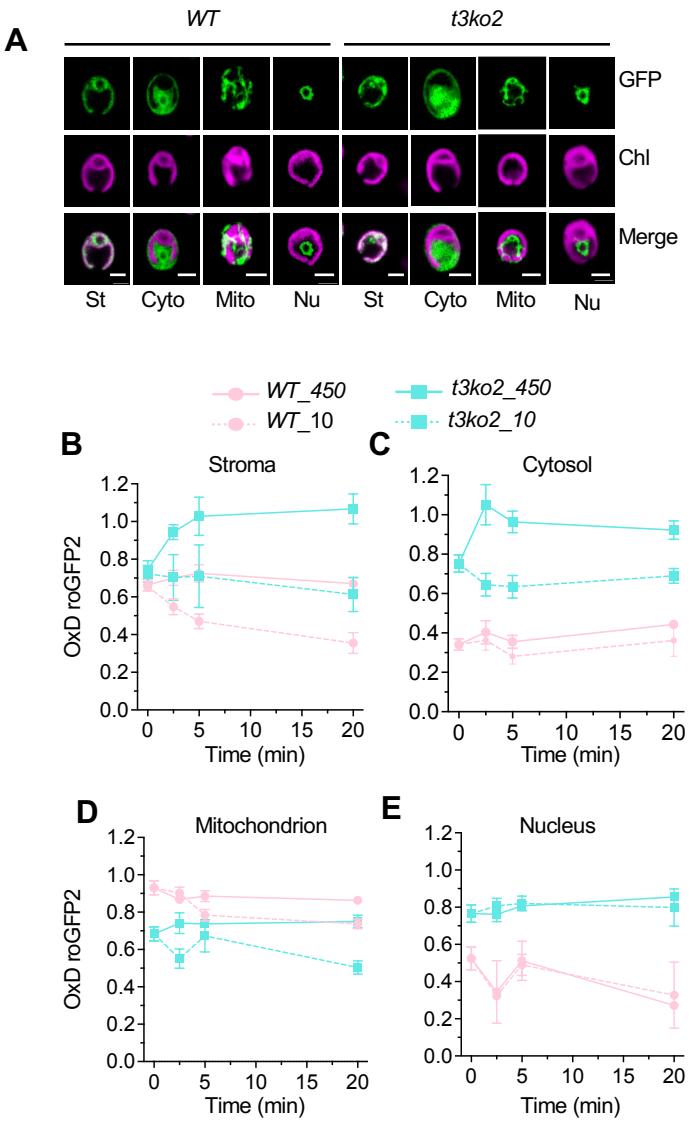

Fig. 6: Real-time monitoring of H_2O_2 compartmentalized distribution in *t3ko2* and WT upon transition from LL to HL. (**A**) The hypersensitive H_2O_2 sensor (roGFP2-Tsa2ΔCR) protein was targeted to the chloroplast stroma (St), cytosol (Cyto), mitochondrion (Mito) and nucleus (Nu). Shown are GFP fluorescence, chlorophyll autofluorescence (Chl) and the two signals merged (scale bar: 5 µm). WT and *t3ko2* transformant cells, accumulating roGFP2-Tsa2ΔCR in the stroma (**B**), cytosol (**C**), mitochondrial matrix (**D**), and nucleus (**E**), were acclimated to LL in TP and then were transferred either to HL (450 µmol photons m^{-2} s^{-1}, solid line) or to very LL (10 µmol photons m^{-2} s^{-1}, dotted line) for 20 min. The oxidation state of the sensor was trapped by the addition of NEM and roGFP2 fluorescence was measured in a plate reader as previously described (Niemeyer et al., 2021). Shown are the mean values from three independent experiments with the error bars representing the standard deviation.

1067

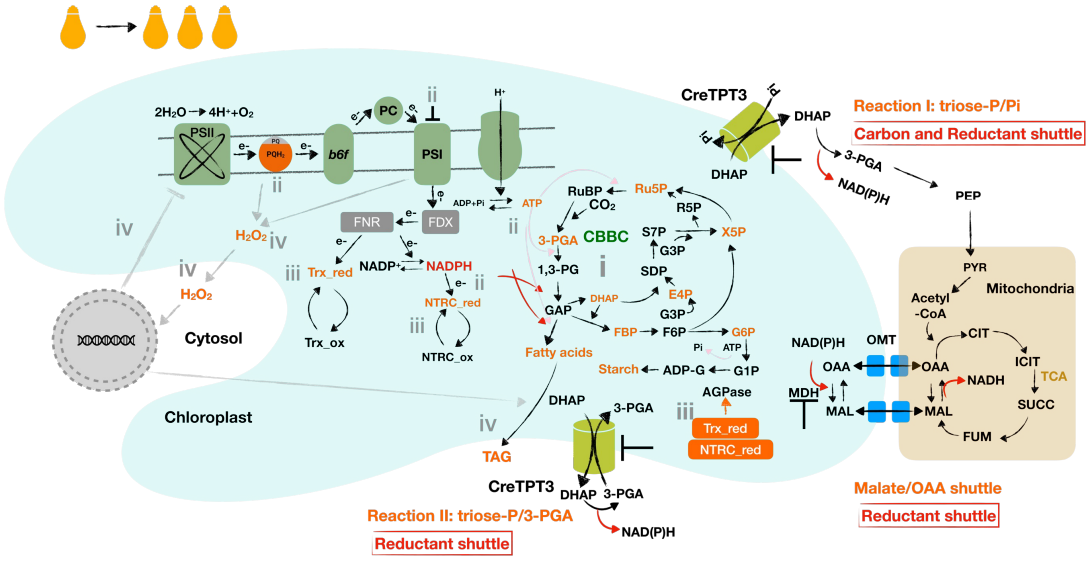

Fig. 7: Impact of eliminating Chlamydomonas TPT3 on the chloroplast metabolic landscape. i. reduced triose-P export leads to accumulation of the sugar-P in CBBC and glycolysis pathways (e.g. triose-P, hexose-P, marked in orange), and an elevated ratio of 3-PGA/Pi (which can allosterically activate AGPase activity) would begin to stimulate the synthesis and accumulation of storage carbon; **ii.** CBBC activity diminishes as a consequence of the hyper-accumulation of the precursors with the fixation of CO_2, leading to elevation of reductant (NADPH) and energy (ATP) within the chloroplast; the elevated NADPH:$NADP^+$ and ATP:ADP ratios, elicit strong feedback on PET causing hyper-reduction of electron carriers (eg: over reduced PQ pool and highly reduced PSI) that slows electron flow across the cytochrome b_6f complex; **iii.** the highly reduced PET system and the elevated NADPH can actively reduce FDX/TRX and the NTRC systems, respectively; reduced TRX and/or NTRC can activate the AGPase (above the activity elicited by an increase in the 3-PGA/Pi ratio), leading to additional starch accumulation; **iv.** hyper-reduction of PET can also lead to stromal ROS accumulation, that can act as a signal that controls expression of chloroplast and nuclear genes; ROS also cause damage to both PSII and I and leads to neutral lipid accumulation as a consequence of activation of diacylglycerol acyltransferases (DGAT) and phospholipid diacylglycerol acyltransferase (PDAT). Many of these metabolic/acclimatory processes both overlap and are interconnected. Under conditions of extended exposure to ML, the damage in Chlamydomonas *tpt3* mutants can accumulate and lead to cell death; cell death occurs rapidly in HL.

1068

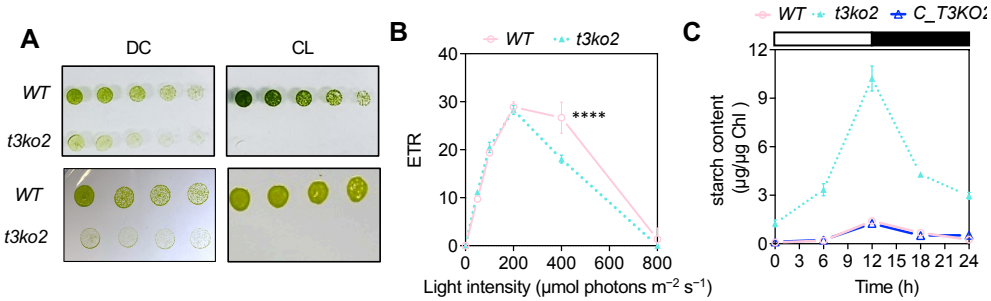

Fig. 8: Effects of deletion of CreTPT3 over diurnal cycle. (**A**) Growth of WT, and *t3ko2* strains on TP agar plates for 4 days either under diurnal cycle (DC) (left panel; light : dark/ 12h : 12h) or continuous light (CL) (right panel) at an intensity of 60 µmol photon $m^{-2}s^{-1}$ (upper panel) or HL (lower panel: 450 µmol photon $m^{-2}s^{-1}$). The dilution series are 3, 1.5, 0.75, 0.375 µg/mL chlorophyll. (**B**) Photosynthetic electron transport rate (ETR) of cells grown under a diurnal rythym with the light period at an intensity of 60 µmol photon $m^{-2}s^{-1}$. (**C**) Accumulation of starch during growth under a diurnal rythym at a light intensity of 60 µmol photon $m^{-2}s^{-1}$.

1069
1070

1071 **Supplementary Materials**

1072 **Materials and methods**

1073 **Expression of CreTPT2 and CreTPT3 in yeast**

1074 The DNA sequence encoding the mature CreTPT2 or CreTPT33 protein was codon-
1075 optimized for expression in *Saccharomyces cerevisiae* (GeneART, ThermoFisher
1076 Scientific). This coding sequence was inserted in frame with an N-terminal His tag into
1077 the yeast vector pYES-NTa (ThermoFisher Scientific) using Gibson cloning (NEB). Briefly,
1078 pYES-NTa was linearized with BamHI and the Cre*TPT2* and *TPT3* cDNA amplified with
1079 the primer pairs: fwd:5'-gacgataaggtacctagcGCTGCTGCTGTTCCAGCTG-3'
1080 and rev: 5'- agaattccaccacactgTTAAGCAGCTTCTGGCTTAACATC-3' (or Cre*TPT2*);
1081 fwd: 5' - gacgataaggtacctagcGCTTCTGCTGCTGATGCTC-3'
1082 and rev: 5' - agaattccaccacactgTTAAGCGGCAGCTGGAGAAG-3' (for Cre*TPT3*). This
1083 cDNA was ligated into the linearized pYES-NTa vector, which was then transformed into
1084 the yeast strain INVSc1 (MATa, his3D1, leu2, trp1-289, ura3-52 / MATa, his3D1, leu2,
1085 trp1-289, and ura3-52, Thermo Fisher Scientific) using the lithium-acetate/PEG method
1086 (Gietz and Schiestl, 2007). Transformed yeast cells were selected on synthetic complete
1087 medium containing 2% (w/v) glucose with the uracil auxotrophic marker. Galactose-
1088 inducible expression of His-CreTPT2 or CreTPT3 in yeast was performed as described
1089 in (Linka et al., 2008). The presence of the His-tagged fusion protein was verified by
1090 standard SDS-PAGE and immunoblot analysis using an anti-His-antibody conjugated
1091 with horseradish peroxidase (Miltenyi Biotech).

1092 **Transport activity assays**

1093 The Km for Pi was determined by measuring the initial velocity at each of six external Pi
1094 concentrations between 0.05 and 5 mM. To obtain competitive inhibition constants (Ki),
1095 the uptake of 0.25 mM Pi into liposomes containing 30 mM Pi was measured over a 4
1096 min period in the presence of increasing external competitor–concentrations (0.05 - 5
1097 mM). Three biological replicates were performed for all described experiments. GraphPad
1098 Prism software version 9.3.0 was used for non-linear regression analyses of the kinetic
1099 data.

1100 **Vector construction**

1101 The plasmid of pRam118_VENUS was linearized with HpaI (NEB). Primers:
1102 g*TPT2*_pRam118_f, g*TPT2*_pRam118_r and g*TPT3*_pRam118_f, g*TPT3*_pRam118_r
1103 (**Supplementary Table 1**) were used to amplify Cre*TPT2* and Cre*TPT3* genomic DNAs
1104 containing an overlap with the linearized pRam118_VENUS vector. For generating the
1105 plasmids pRam118-CreTPT2&VENUS and pRam118-CreTPT3&VENUS, genomic DNA
1106 of Cre*TPT2* or Cre*TPT3* was assembled with pRam118_VENUS plasmid using Gibson
1107 assembly (Gibson et al., 2009). The plasmid of pRam118-CreTPT2&VENUS (2-4 µg)

1108 linearized with AseI (NEB), was transferred into the Chlamydomonas M10 strain by
1109 electroporation.

1110 A 1,000 bp sequence upstream of Cre*TPT3* and containing the promoter region of the
1111 gene was amplified using the primers TPT3pro1000_f and TPT3pro1000_r
1112 (**Supplementary Table 2**). The 3' UTR of Cre*TPT3* was amplified using TPT_3UTR_f
1113 and TPT3_3UTR_r (**Supplementary Table 2**). The *PSAD* promoter and the *RBCS2*
1114 3'UTR of pRam118-CreTPT3&VENUS were replaced by the amplified fragments of the
1115 1,000 bp upstream region and the 3' UTR of Cre*TPT3*, respectively. This final vector,
1116 designated pRam118_CreTPT3, contains the original Cre*TPT3* promoter (driving
1117 expression of Cre*TPT3*), the genomic DNA sequence of Cre*TPT3*, VENUS and the
1118 Cre*TPT3* 3' UTR plus the *AphVII* cassette. To locate CreTPT3 and complement the *tpt3*
1119 mutant, the mutant was transformed by electroporation with a total amount of 2-4 µg
1120 (~500 ng/µL) of pRam118_CreTPT3 that was linearized with AseI.

1121 **CRISPR-Cas9 mediated mutagenesis**

1122 Prior to electroporation, Cas9 (IDT) and sgRNAs were incubated together at 37 °C for
1123 30 min. Approximately 500 ng PCR product of the *AphVII* cassette, which confers
1124 resistance to hygromycin, was added to the RNP (ribonucleoprotein) mixture. 250 µl
1125 aliquots were electroporated using Super Electroporator NEPA21 type II (NEPA GENE).
1126 After 16 h of recovery in very low light (10-15 µmol photons m^{-2} s^{-1}), cells were plated onto
1127 solid TAP medium containing 10 µg/mL hygromycin. Sense or antisense-oriented knock-
1128 ins of *AphVII* were determined by amplification using primer pairs with one primer
1129 annealing to the genomic sequence and the other to the inserted sequence
1130 (**Supplementary Table 2**). The amplified fragments were sequenced to verify the
1131 insertion sites (ELIM BIOPHARM, Hayward, USA).

1132 **ROS measurements and roGFP2 imaging analysis**

1133 Briefly, after various treatment (e.g. 48 h in ML), 10 million Chlamydomonas cells were
1134 pelleted and washed once with 1×PBS. The cells were then resuspended in 1×PBS
1135 containing 8 µM CM-H2DCFDA and incubated at room temperature in the dark for 30 min.
1136 Following this incubation, the cells were washed three times with 1×PBS buffer, the
1137 fluorescent signals were either visualized using TCS SP8 confocal laser-scanning
1138 microscope (Leica) or quantified with a microplate reader (Infinite M1000; TECAN).
1139 Excitation and emission settings for the microscope were: 488 nm/510-530 nm HyD SMD
1140 hybrid detector for reactive oxygen species (ROS), and 488 nm/650-700 nm-HyD SMD
1141 hybrid detector for chlorophyll autofluorescence. Excitation and emission settings for the
1142 plate reader were as follows: ROS excitation 488/5 nm and emission 530/12 nm;
1143 chlorophyll excitation 514/5 nm and emission 690/5 nm.

1144

1145 **Starch analysis**

1146 In brief, cells were collected by centrifugation and pigments extracted with methanol.
1147 Dried pellets were resuspended in water and heated at 100°C to break the cells and
1148 release the starch. After cooling, amyloglucosidase and α-amylase (2.25 U/mL) were
1149 used to hydrolyze the starch and the products of hydrolysis were quantified using a
1150 Glucose Colorimetric Detection Kit (Thermo Fisher).

1151 **Photosynthesis-Irradiance curve**

1152 The YSI 5331A electrodes (Yellow Springs Instruments) were polarized at −0.8 V. The
1153 cultures used for the assays were concentrated to 2.5-5 μg mL^{-1} chlorophyll,
1154 supplemented with 15 μL of 0.5 M sodium bicarbonate in water and then purged with 1%
1155 CO_2/99% He. Using a gas tight syringe, the sample was transferred into the reaction
1156 chamber that was also purged with 1% CO_2/99% He. The rate of change in O_2 levels was
1157 measured sequentially at the light intensities 100, 200, 600, 1000 μmol photons m^{-2} s^{-1}
1158 (photosynthetic active radiation, PAR); each intensity was maintained for 3-5 min followed
1159 by a 3-min intervening dark period, and then the light level was raised to the next higher
1160 intensity (stepped change) until the full range of intensities was tested. At 1,000 μmol
1161 photons m^{-2} s^{-1}, the light was held for 10 min followed by an 8-min dark period. Before the
1162 measurement of each experimental series, the electrodes were calibrated with air (~21%
1163 O_2) and 1% CO_2/99% He mixture (0% O_2). The initial slope of the response was used to
1164 determine the O_2 evolution rate.
1165

1166 **Extraction of samples for LC-MS/MS**

1167 The quenching solution, filtered saline (9 g/L NaCl), was prechilled to 4°C in a refrigerator.
1168 30 mL of the quenching solution was transferred to a 50 mL conical tube kept in an ice
1169 bath mixed with salt to depress the temperature to between -3 °C and -1 °C. 15 mL of the
1170 culture was rapidly plunged into the 30 mL of the quenching solution and the samples
1171 were centrifuged at 4,000 rpm for 10 min at 4 °C. Cell pellets were washed with fresh
1172 prechilled saline solution and centrifuged again at 4,000 rpm for 10 min in a 2 mL
1173 centrifuge tube. For each replicate, 45 mL of the culture was sampled and the cell pellets
1174 were pooled. Washed pellets were frozen at -80 °C until extraction. Metabolite extraction
1175 and further analysis were modified from (Young et al., 2011). To each cell pellet, 500 μL
1176 methanol was added along with the internal standards ribitol and PIPES to a final
1177 concentration of 2 μM each. Samples were then vortexed for 30 sec, frozen in liquid
1178 nitrogen as described in (Winder et al., 2008), and allowed to thaw at 0 °C. This vortex-
1179 freeze-thaw cycle was repeated twice more before the samples were centrifuged at
1180 10,000 x g at 1 °C for 5 min. The supernatant was collected, and the remaining pellets
1181 were extracted twice more with 500 μL of a 50:50 mixture of methanol and water, with 3
1182 vortex-freeze-thaw cycles done for each extraction. Supernatants from each extraction
1183 procedure were pooled and dried on a Thermo Fisher SpeedVac Concentrator. Dried

1184 extracts were then resuspended in 500 µL water and cleaned to remove any residual
1185 large cell debris by filtration, first through a 0.22 µm pore size Spin-X centrifugal tube filter,
1186 followed by 10 K molecular mass cutoff filters, followed finally by 3 K molecular mass
1187 cutoff filters. After each filtration step, filters were rinsed with 50 µL water, which was
1188 added to the total sample volume for subsequent steps. Filtered extracts were dried again
1189 and resuspended in 200 µL water for LC-MS/MS analysis.

1190 **Protein extraction and immunoblot analysis**

1191 Affinity-purified polyclonal antibodies to CreTPT3 were custom-made by GenScript. The
1192 antigen sequence used for antibody generation was KSWSFGRPVTKQEF.
1193 Chlamydomonas cells were grown in liquid cultures to 2–5 x10^6 cells ml^{-1} and collected
1194 by centrifugation (1459 x g, 5 min). Cells were resuspended in resuspension buffer [(5
1195 mM HEPES, pH 7.5, KOH), 10 mM EDTA (pH 7.5, NaOH), 1x protease inhibitor "complete
1196 EDTA-free" (Roche)]. For the disruption of cells, bead-beating was performed using a
1197 mini beadbeater (Biospec) in two cycles of 30 sec min^{-1}, with a 1 min period of cooling on
1198 ice between cycles. Disrupted cells were centrifuged at 4 °C, 30 min, 14000 x g in a
1199 microfuge. The supernatant was removed, the pellet was resuspended in sample buffer
1200 (resuspension buffer supplemented with 100 mM Na_2CO_3, 100 mM DTT, 2% WT/vol SDS,
1201 and 12% WT /vol sucrose).

1202 SDS-PAGE was performed using a 12% polyacrylamide gel (Bio-Rad), with the
1203 electrophoresis for 90 min at 120 V. The proteins within the gel were transferred onto a
1204 PVDF membrane (Bio-Rad) using Trans-Blot Turbo (Bio-Rad). The detection was
1205 performed using Clarity Max Western ECL Substrate (Bio-Rad).

1206 **RT-qPCR**

1207 RT-qPCR, was performed as described previously (Kaye et al., 2019). Briefly, total RNA
1208 was isolated using the RNeasy Plant Mini Kit (Qiagen) and treated with DNase I (Qiagen).
1209 First-strand cDNA was generated by reverse transcription of 0.5 µg total RNA using the
1210 iScript cDNA Synthesis Kit (Bio-Rad). Real-time PCR using the Roche Light Cycler 480
1211 was performed with the SensiMix NO-Rox SYBR Green I Kit as described by the
1212 manufacturer (Bioline). Oligos used in this research for analyzing the expression levels
1213 of Cre*TPT10/TPT2/TPT3/CGL51* are listed in **Supplemental Table 1**. *mRNA levels were*
1214 *calculated using DeltaC (T) method, CBLP gene was used as an internal control.*

1215 **Analysis of transcript levels in response to different conditions**

1216 In order to analyze the transcript level of Cre*TPT* genes under different conditions, we
1217 obtained RNAseq data published previously in which cells experienced a diurnal cycle,
1218 nitrogen starvation, sulfur starvation and Fe^{2+} starvation (Strenkert et al., 2019; Zones et
1219 al., 2015; Ngan et al., 2015; González-Ballester et al., 2010; Urzica et al., 2013). The log2

1220 fold change of each gene was calculated based on the ratio of transcript abundance at
1221 different time point over transcript level at time point 0 h. The fold change was visualized
1222 by a heatmap and the color bar is the scale of log2 (fold-change).

1223 **Correlation analysis based on Cre*TPT3* transcription abundance under different**
1224 **conditions**

1225 The Z score of each gene was calculated as follows: the mean transcript level of each
1226 gene from all of the conditions was subtracted from each gene's transcript level. This
1227 difference was divided by the standard deviation of each gene's transcript level under all
1228 conditions to get Z score numeric values. The whole Z score matrix for every gene under
1229 all conditions was used to calculate the Pearson correlation matrix by using python.
1230 Dataframe.corr() function. The genes highly correlated with TPT3 were selected if their
1231 correlation value is higher than 0.75. The Pearson correlation value of TPT3-highly-
1232 correlated genes were plotted based on their KEGG pathway.

1233 **In vivo polymeric carbohydrate staining**

1234 Lugol's iodine (aqueous solution of 1.8% iodine and 3.0% potassium iodide) was used to
1235 stain in vivo polymeric carbohydrate. Briefly, 0.5 mL of the cell culture was pelleted,
1236 resuspended in 10 μL of Lugol's iodine and visualized under a bright-field microscope.
1237 Lugol's iodine selectively binds to alpha-1,4 glucans and stains it blue-black.

1238

1239

1240

1241

1242

1243

1244

1245

1246

1247

1248

1249 **Supplementary Tables**

Cre ID	Name from V6.1 / (name used in this study)	Previous name	Prediction	CS Position
Cre08.g379350_4532	**TPT10 / (TPT10)**	**TPT1**	**cTP**	**CS pos: 61-62. TCL-AV. Pr: 0.3994**
Cre06.g263850_4532	**N / (TPT2)**	**PPT2; TPT2; TPT20**	**cTP**	**CS pos: 70-71. VCQ-AA. Pr: 0.5253**
Cre01.g045550_4532	**TPT3 / (TPT3)**	**TPT3**	**cTP**	**CS pos: 60-61. VTK-AS. Pr: 0.4178**
Cre02.g106200_4532	N	TPT4; TPT5	OTHER	
Cre02.g112900_4532	N	TPT5; TPT6	OTHER	
Cre02.g144300_4532	N	TPT6; TPT7	OTHER	
Cre03.g162000_4532	N	TPT7; TPT8	OTHER	
Cre03.g184850_4532	N	TPT8; TPT9	OTHER	
Cre04.g227450_4532	N	TPT9	OTHER	
Cre07.g330850_4532	N	TPT10; TPT11	OTHER	
Cre08.g363600_4532	N	TPT11; TPT12	OTHER	
Cre09.g408400_4532	N	TPT12; TPT13	OTHER	
Cre09.g413700_4532	N	TPT13; TPT14	OTHER	
Cre08.g382350_4532	EZY14	TPT14; TPT16; EZY14	OTHER	
Cre09.g415900_4532	MOT20	TPT15	OTHER	
Cre10.g452750_4532	N	TPT16; TPT18	OTHER	
Cre11.g479950_4532	CGL7	TPT17	OTHER	
Cre12.g490050_4532	N	TPT18; TPT19; GMT1	OTHER	
Cre12.g490100_4532	TPT2	TPT19;GMT2	OTHER	
Cre12.g501000_4532	N	TPT20; TPT22; PPT1	OTHER	
Cre15.g641266_4532	N	TPT22; TPT23	OTHER	
Cre15.g642950_4532	N	TPT23; TPT24	OTHER	
Cre15.g643385_4532	N	TPT24; TPT26	OTHER	
Cre16.g663800_4532	**CGL51 / (CGL51)**	**TPT25**	**cTP**	**CS pos: 70-71. IVA-SS. Pr: 0.4817**
Cre16.g666250_4532	N	TPT26; TPT27	OTHER	
Cre17.g702700_4532	N	TPT27; TPT28	OTHER	
Cre17.g703250_4532	SLC35D	TPT28; TPT29	OTHER	
Cre17.g710850_4532	N	TPT29; TPT4	OTHER	
Cre11.g467754_4532	N	UAA6	OTHER	
Cre14.g622700_4532	N	N	OTHER	
Cre18.g748947_4532	N	N	OTHER	
Cre09.g408428_4532	N	N	OTHER	

1250

1251 **Supplementary Table 1: Members of the triose phosphate transporter family in**
1252 ***Chlamydomonas reinhardtii* and their predicted subcellular localization based on TargetP-**
1253 **2.0.** cTP, chloroplast transit peptide; CS position, cleavage site of transit peptides; N: genes
1254 without names in the genome. Cre IDs are from v6.1 genome.

oligo name	sequence
gTPT2_pRam118_f	tactcacaacaagcccagttatggcgtctctgctgggc
gTPT2_pRam118_r	gagccacccagatctccgttggcggcctccggcttgac
gTPT3_pRam118_f	tactcacaacaagcccagttATGGCTTCGCTCGCTCAGCGCGTGAGC
gTPT3_pRam118_r	gagccacccagatctccgttGGCCGCGGCCGGCGACGC
TPT3pro1000_f	gccttttgctcacatgtggcggccgccgccatgctggccaacag
TPT3pro1000_r	taccaatccacaaatgtgggctagcccatgtgaaggcgttgacc
TPT3_3UTR_f	gatgacgacaagtaaagatctTAAGGCGGGCAGCGGC
TPT3_3UTR_r	GCGCAAGAAAGAAGCTTGATATCCCCCTTATAATGTTTACAAGTGGTGCG
hygro_crispr_f2	GGAACTGGCGCAGTTCCTCTG
hygro_crispr_re2	GGCTCGCGTAGGAATCATCCG
TPT2_gRNA1_F	TGGGACGGGAGGTGGAGAGC
TPT3_gRNA1_F	GCTCGGTTGAGCGCACCC
TPT3_gRNA1_R	CAAGGGTCTGGCGAGCACG
TPT3_gRNA2_F	ACCTCCCCATCGCCACGAT
TPT3_gRNA2_R	AGGGGTAAGGACAGCGGTG
Qrt_TPT10_f	CCTGTACCAGCAGGTGTCGTAC
Qrt_TPT10_r	CCAGCGCGTTCTGGAGTGACA
Qrt_TPT2_f	ATGGCGTCTCTGCTGGGC
Qrt_TPT2_r	CTGCTCGCCCATTCTCCTC
Qrt_TPT3_f	GCAAAGCTGGCGCCTACTG
Qrt_TPT3_r	TAGACCAGGCCGACCACCAC
Qrt_CGL51_f	CTGGTTCATCGGGACATGGC
Qrt_CGL51_r	TGGCTGAAGCTGACCACT
Qrt_MDH1_f	GGCTCTGCTGCTGAAGATGAAC
Qrt_MDH1_r	CGGTGTAGCCAGTAACCTTCAC
Qrt_MDH5_f	GGCCCTGAACATGAAGCAGC
Qrt_MDH5_r	GGCGGAAGACTCCATAGGCC

Supplementary Table 2: Oligonucleotide list.

ID	Construct	Restriction enzyme for transformation	Localization
pMBS472	PSADpro::aadA::PSAD-T:::: ARpro::roGFP2-Tsa2ΔCR::MStop::RPL23-T	ECoRV/AfeI	cytosol
pMBS652	PSADpro::aadA::PSAD-T:::: ARpro::CDJ1::roGFP2-Tsa2ΔCR::MStop::RPL23-T	ECoRV/AfeI	stroma
pMBS657	PSADpro::aadA::PSAD-T:::: ARpro::roGFP2-Tsa2ΔCR::SV40::RPL23-T	ECoRV/AfeI	nucleus
pMBS655	PSADpro::aadA::PSAD-T:::: ARpro::HSP70C::roGFP2-Tsa2ΔCR::MStop::RPL2	ECoRV	mitochondrion

Supplementary Table 3: Plasmids of H_2O_2 roGFP2-Tsa2ΔCR sensors (Niemeyer et al., 2021)**.**

Name	Cre number	Gene function	Correlation coefficient	Localization
TPT3	Cre01.g045550	Triose phosphate/phosphate translocator 2	1	chloroplast
AMY	Cre08.g362450	Alpha-amylase	0.881792677	chloroplast
SP	Cre07.g336950	Starch phosphorylase	0.861504451	chloroplast
ISA3	Cre03.g207713	Isoamylase, starch debranching enzyme	0.790501386	chloroplast
PGI1	Cre03.g175400	Phosphoglucose isomerase	0.808137223	chloroplast
PFK2	Cre12.g553250	Phosphofructokinase	0.805294876	chloroplast
PGM1	Cre06.g272050	Phosphoglycerate mutase	0.838232423	other
IDH2	Cre02.g143250	Isocitrate dehydrogenase, NAD-dependent	0.81622058	other
MDH4	Cre12.g483950	Malate dehydrogenase 4	0.80363604	mitochondrion
PDH1	Cre16.g677026	Pyruvate dehydrogenase E1 beta subunit	0.805186998	mitochondrion
ASAP3	Cre07.g338050	Mitochondrial F1F0 ATP synthase associated protein 3	0.853067434	mitochondrion
MPPB	Cre12.g523850	Mitochondrial processing peptidase beta subunit and Complex III Core I subunit	0.844453019	mitochondrion
NUO5	Cre10.g450400	NADH dehydrogenase (ubiquinone) flavoprotein 2,mitochondrial(respiratory Complex I)	0.781322987	mitochondrion
NUO6	Cre10.g422600	NADH:ubiquinone oxidoreductase 51 kDa subunit,mitochondrial, respiratory Complex I	0.770479958	mitochondrion
COX2a	Cre03.g154350	Mitochondrial cytochrome c oxidase subunit II	0.824639841	mitochondrion
COX2	Cre01.g049500	Mitochondrial cytochrome c oxidase subunit II, protein IIb of split subunit	0.814345856	mitochondrion
COX3	Cre04.g221700	Mitochondrial cytochrome c oxidase subunit III	0.813942712	mitochondrion
COX90	Cre16.g691850	Cytochrome c oxidase subunit Cox90, mitochondrial	0.803959451	mitochondrion
COX10	Cre12.g516350	Mitochondrial cytochrome c oxidase assembly protein	0.770332065	mitochondrion
ATP1a	Cre02.g116750	Mitochondrial F1F0 ATP synthase, alpha subunit	0.850554844	mitochondrion
ATP2	Cre17.g698000	Mitochondrial F1F0 ATP synthase, beta subunit	0.839116637	mitochondrion
ATP3	Cre15.g635850	Mitochondrial F1F0 ATP synthase, gamma subunit	0.790390859	mitochondrion
ATP4	Cre11.g467707	Mitochondrial F1F0 ATP synthase, delta subunit	0.782621502	mitochondrion
ASA7	Cre09.g416150	Mitochondrial F1F0 ATP synthase associated protein 7	0.762529504	mitochondrion
ATP5	Cre16.g680000	Mitochondrial ATP synthase subunit 5	0.75995889	mitochondrion
CYC1	Cre15.g638500	Ubiquinol:cytochrome c oxidoreductase cytochrome c1,mitochondrial	0.78087886	mitochondrion
OMT1	Cre17.g713350	Oxoglutarate:malate antiporter1	0.7724107	chloroplast
MDH1	Cre03.g194850	NAD-dependent malate dehydrogenase	0.770420148	chloroplast
ANT1	Cre09.g386650	ADP/ATP carrier protein, mitochondrial	0.841663755	mitochondrion
AAA1	Cre08.g358526	Plastidic ADP/ATP translocase	0.831658774	chloroplast
ATPva3	Cre04.g220350	Vacuolar ATP synthase subunit A	0.806662753	other
VTC1	Cre12.g510250	Vacuolar Transport Chaperone-like protein	0.753558866	other
PST1	Cre07.g331550	Phosphoserine aminotransferase	0.787494263	chloroplast
CPL12	Cre10.g466500	Glyoxalase	0.787085275	chloroplast
NAGSAD	Cre03.g146187	N-acetyl-gamma-glutamyl-phosphate reductase / NAGSA dehydrogenase/oxidoreductase	0.772201917	chloroplast
NAGK1	Cre01.g015000	Acetylglutamate kinase/L-arginine biosynthesis II (acetyl cycle)	0.771816595	chloroplast
PFGS	Cre08.g364800	Phosphoribosylformylglycinamidine synthase /superpathway of purine nucleotides	0.761886415	chloroplast
PPP2r2	Cre01.g055420	serine/threonine-protein phosphatase 2A regulatory subunit B	0.776264136	chloroplast
CLTC	Cre02.g101400	clathrin heavy chain	0.775380317	other
SLC40a1	Cre06.g251000	solute carrier family 40	0.771233669	secretory pathway

Supplementary Table 4: List of genes with strong Pearson correlation to *CreTPT3*.

Supplementary Figures

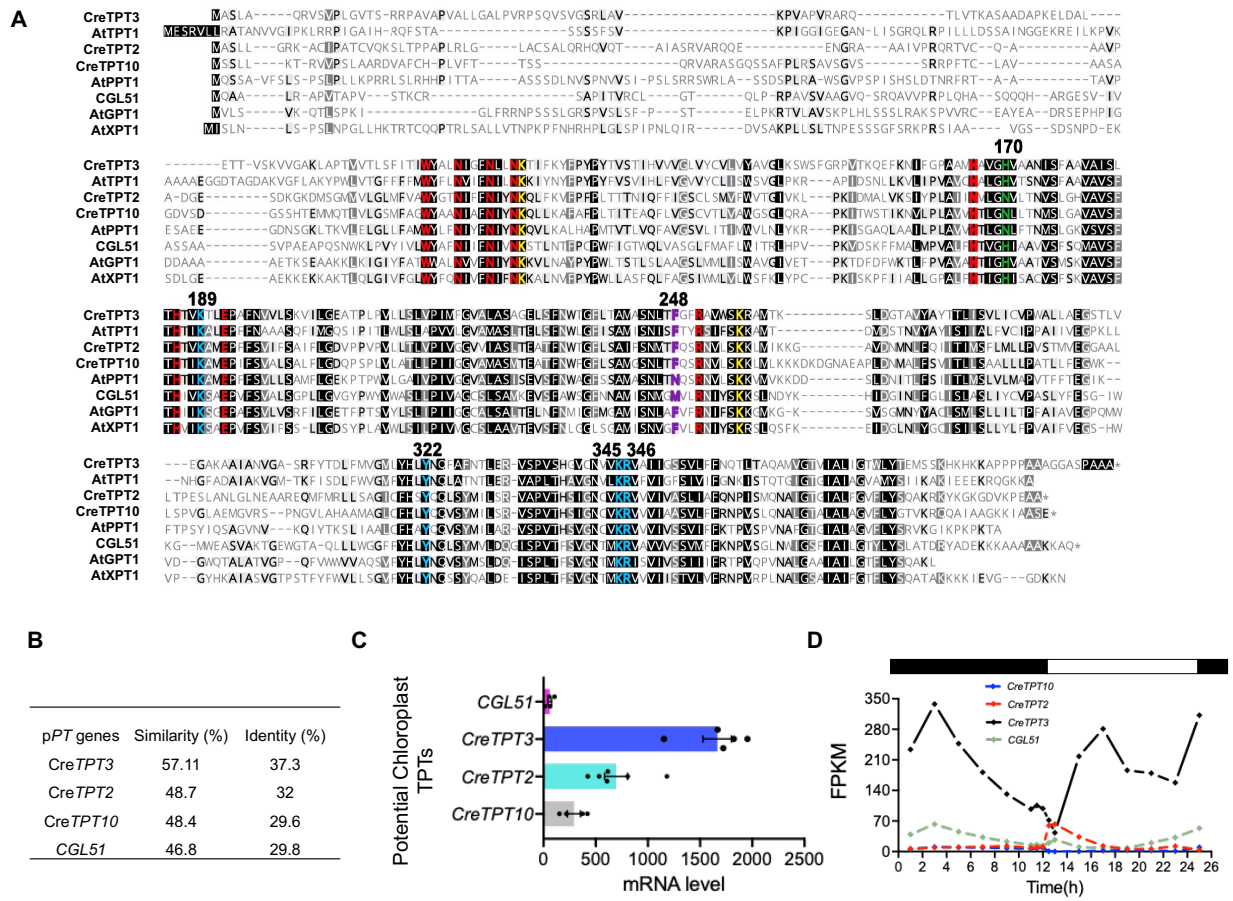

pPT genes	Similarity (%)	Identity (%)
Cre*TPT3*	57.11	37.3
Cre*TPT2*	48.7	32
Cre*TPT10*	48.4	29.6
CGL51	46.8	29.8

Supplementary Fig. 1: Features of putative plastid phosphate transporter (pPT) in *Arabidopsis thaliana* and *Chlamydomonas reinhardtii*. (**A**) Alignment of sequences of pPTs in Arabidopsis and Chlamydomonas. Plastid putative sugar phosphate transporters from Chlamydomonas are CreTPT10 (Cre08.g379350_4532), CreTPT2 (Cre06.g263850_4532), CreTPT3 (Cre01.g045550_4532), and CGL51 (Cre16.g663800_4532). Sequences from *Arabidopsis thaliana* are AtTPT1 (AT5G46110.1), AtPPT1 (AT5G33320.1), AtGPT1 (AT5G54800.1) and AtXPT1 (AT5G17630.1). Conserved substrate binding pockets are colored red. Phosphate-binding residues are colored blue. The gate capping residues are colored yellow. The positions of residue in green are crucial for the substrate preference of either triose-phosphate or 3-PGA. The purple residues are critical for the specificity of PEP. (**B**) The similarity and identity of the protein sequences between Chlamydomonas pPTs and Arabidopsis TPT1. The similarity and identity were calculated using https://www.bioinformatics.org/sms2/ident_sim.html. (**C**) mRNA levels encoding putative chloroplast envelope localized pPTs under LL during growth in TP medium. (**D**) Expression of pPTs over the diel cycle; data was extracted from Zones et al., 2015. Supports Fig. 1 and 2.

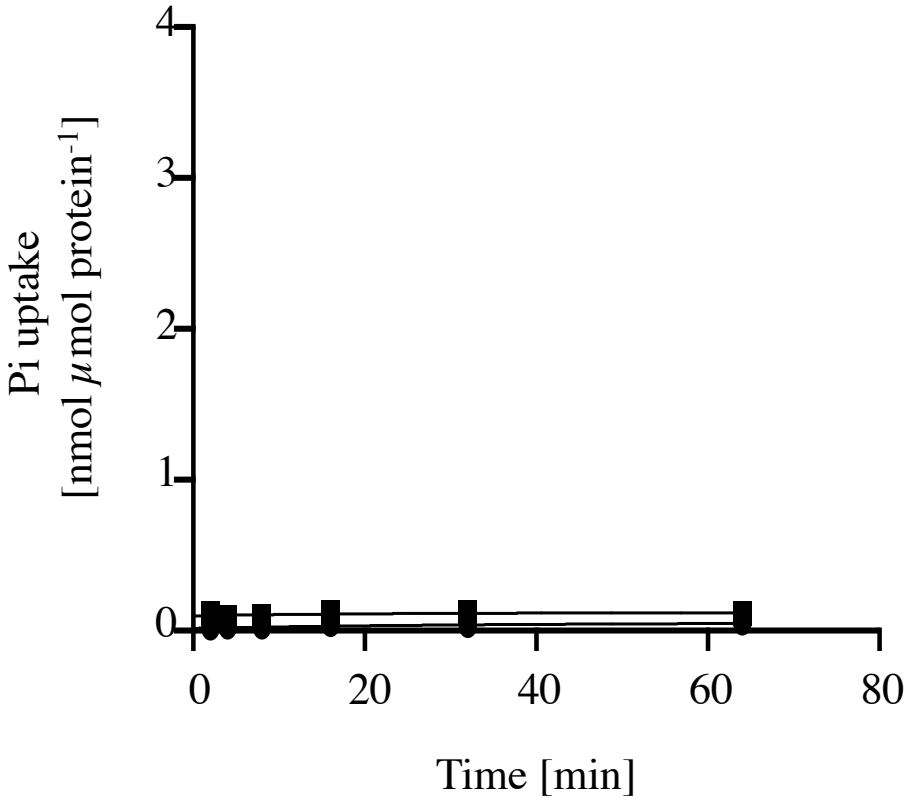

1281

1282 **Supplementary Fig. 2: Background activity of Pi uptake with the endogenous yeast**
1283 **transporters reconstituted in into liposomes.** Time-dependent uptake of Pi (0.25 mM) into
1284 reconstituted liposomes preloaded with 30 mM of Pi (■) or without exchange substrate (●)
1285 prepared from yeast cells harboring the empty vector (pYES-NTa). The arithmetic mean (±SD) of
1286 three independent experiments (each with three technical replicates) was plotted against time.
1287 The observed Pi uptake rates of endogenous yeast carriers reconstituted into liposomes were
1288 negligible compared to the rates with His-CreTPT2/3 (20-fold higher, **Fig. 1C, D**), indicating that
1289 this expression system is suitable for functional analysis of recombinant phosphate transporters.
1290 Supports Fig. 1.

1291

Supplementary Fig. 3: Mutations generated in the Cre*TPT2* gene by CRISPR-Cas9 mediated insertion. (**A**) Presentation of the orientation and position of *AphVII* cassette in the Cre*TPT2* gene in *t2ko1*, *t2ko2*, *t2ko3* and *t2ko4*. Sequencing of genomic DNA fragments across the site of *AphVII* cassette in *t2ko1* (**B**) and *t2ko2, t2ko3* and *t2ko4* (**C**). The mismatched nucleotides are marked in pink. Deletions are shown with dashes. (**D**) Growth of WT, *t2ko1*, *t2ko2*, *t2ko3* and *t2ko4* at various dilutions on agar plates with TP or TAP medium and incubated under LL and HL for 6 d. The dilution series used was 1, 0.5, 0.25, 0.125 µg/mL chlorophyll (left to right). Supports Fig. 2.

Supplementary Fig. 4: Types of mutations generated in the Cre*TPT3* gene by CRISPR-Cas9 mediated insertion with sgRNA1 in exon1 and sgRNA2 in exon7. Sequencing of genomic DNA fragments across the site of insertion of *AphVII* cassette in *t3ko1* (**A**) *t3ko2* (**B**) and *t3ko3* (**C**). The orientation and position of *AphVII* cassette are presented above the alignment. The mismatched nucleotides are marked in pink. Deletions are shown with dashes. Supports Fig. 2.

1310

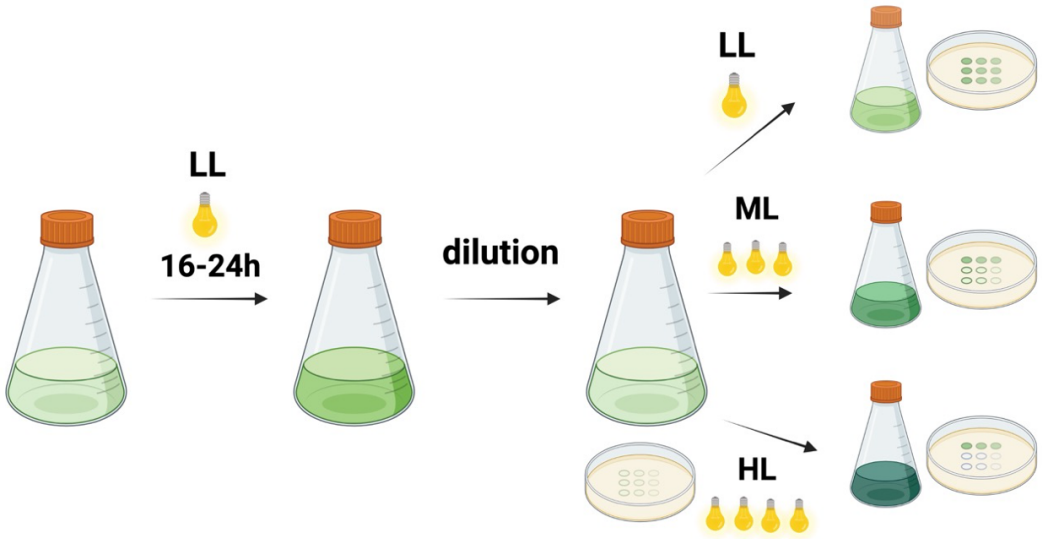

1311

1312 **Supplementary Fig. 5: Experimental set up.** All strains were grown photoautotrophically under
1313 low white light (LL, 30 µmol photons m^{-2} s^{-1}) for 16-24 h. After dilution with fresh medium, the
1314 cultures from LL were then either spotted onto solid medium or to liquid medium and maintained
1315 at either LL, moderate light (ML, 250-300 µmol photon m^{-2} s^{-1}) or high light (HL, 450 µmol photon
1316 m^{-2} s^{-1}) for 24 or 48 h. To avoid self-shading, the culture density was adjusted to 1-1.5 µg/mL
1317 chlorophyll before exposure to ML or HL. Supports Fig. 2,3,4,5.

1318

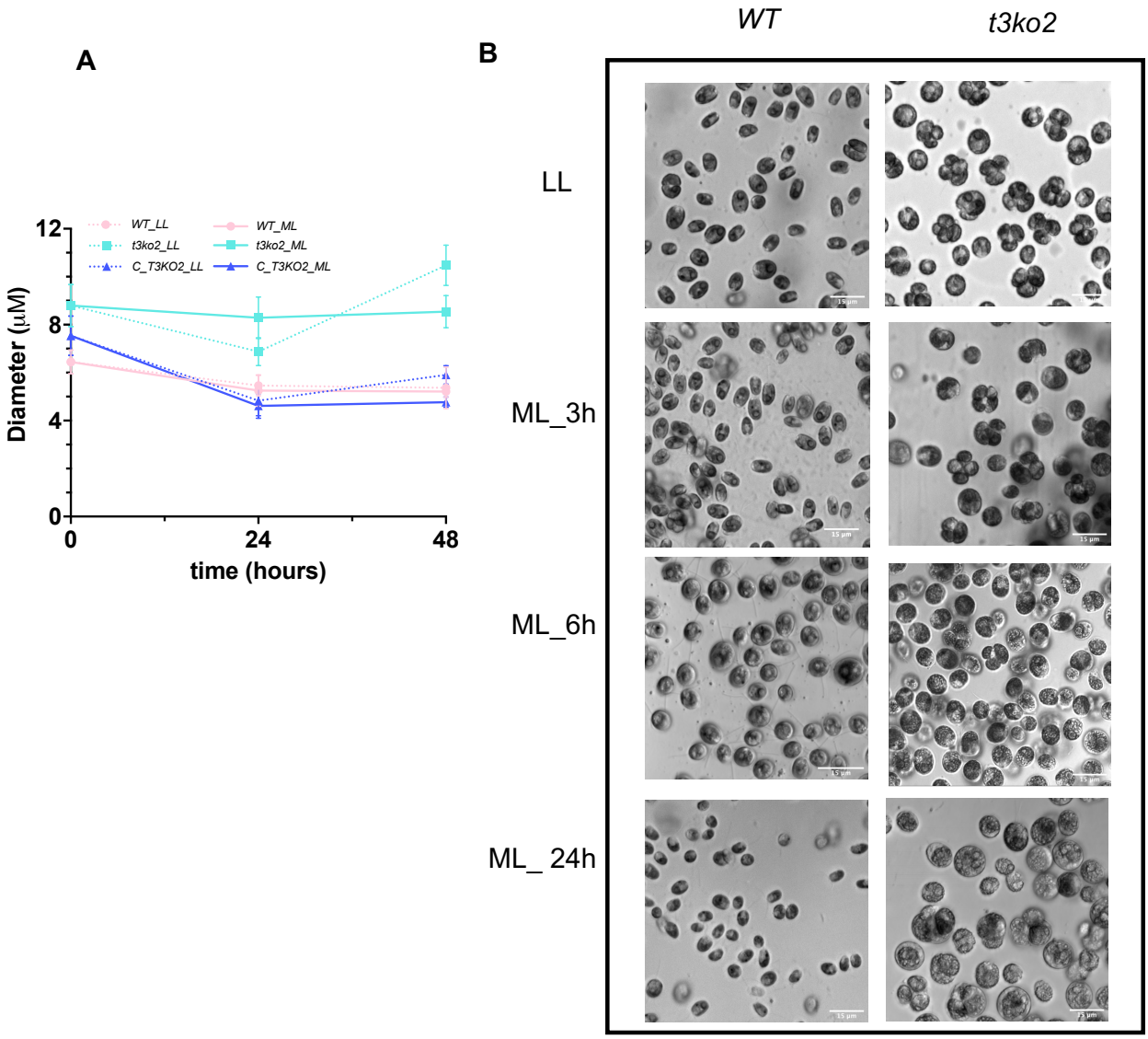

Supplementary Fig. 6: (**A**) Cell size of WT, *t3ko2*, and *C_T3KO2* in TP in both LL and ML. (**B**) WT and *t3ko2* morphology 24 h following a LL to ML transition. Supports Fig. 2.

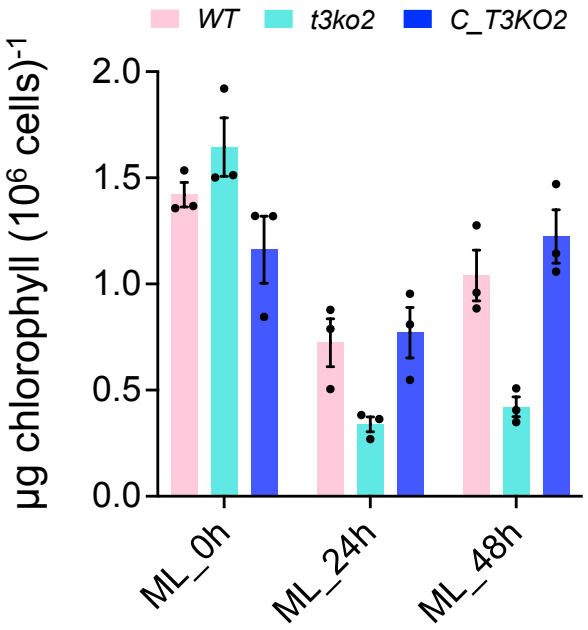

1322

1323 **Supplementary Fig. 7: Quantification of chlorophyll contents in indicated strains after**
1324 **exposure to ML for 24 and 48 h.** All strains were grown photoautotrophically in LL for 16-24 h.
1325 After dilution with fresh medium, the culture was transferred to ML and the chlorophyll content
1326 determined after 24 and 48 h in the ML. The initial inoculum density used for the transition was
1327 between 1-1.5 µg/mL chlorophyll in order to avoid self-shading. Supports Fig. 2.

1328

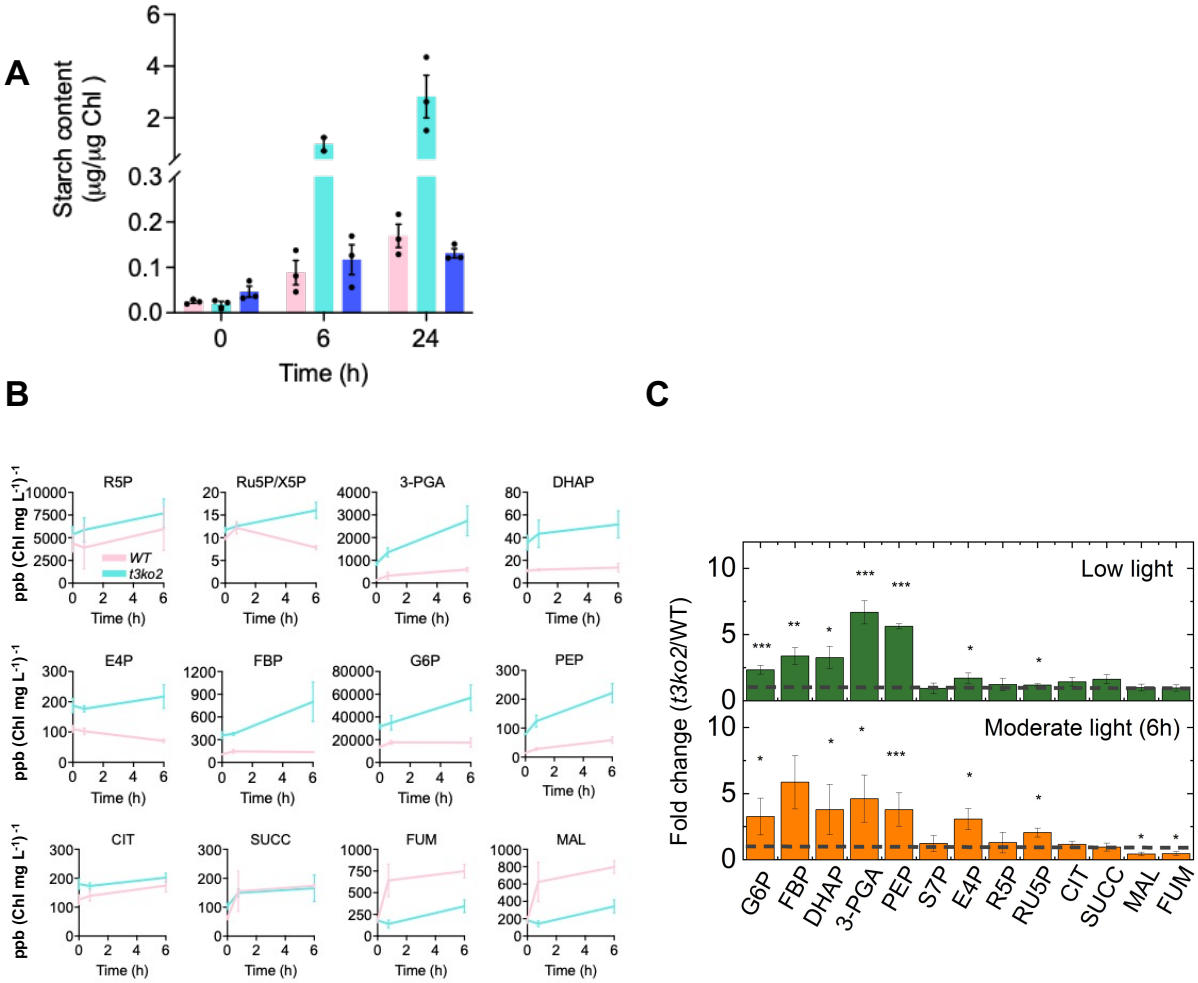

Supplementary Fig. 8: Starch and metabolites in WT and *t3ko2*. (**A**) Starch content in indicated strains following 0, 6, and 24 h in LL. (**B**) Time course, over a period of 6 h, of changes in metabolite pool sizes measured at 0 h (LL), 45 min and 6 h after shifting LL-grown cells to ML. Data was normalized to chlorophyll contents. (**C**) Schematic representation of the fold-change for the metabolites shown in (**B**), calculated by dividing the pool size in *t3ko2* by that of WT cells under the same conditions. Fold change of 1 (no change) is shown by a dashed line. Each data point is the mean and standard error of three biological replicates. ppb: parts per billion. Asterisk indicates statistically significant differences relative to WT (* P<0.05, ** P<0.01, *** P<0.001). Abbreviations: G6P, glucose-6-phosphate; FBP, fructose bisphosphate; DHAP, dihydroxyacetone phosphate; 3-PGA, 3-phosphoglycerate; PEP, phosphoenolpyruvate; CIT, citrate; SUCC, succinate; FUM, fumarate; MAL, malate; S7P, sedoheptulose-7-phosphate; E4P, Erythrose 4-phosphate; R5P, Ribose 5-phosphate; RU5P/X5P, ribulose 5-phosphate/xylulose-5-phosphate. Supports Fig. 3.

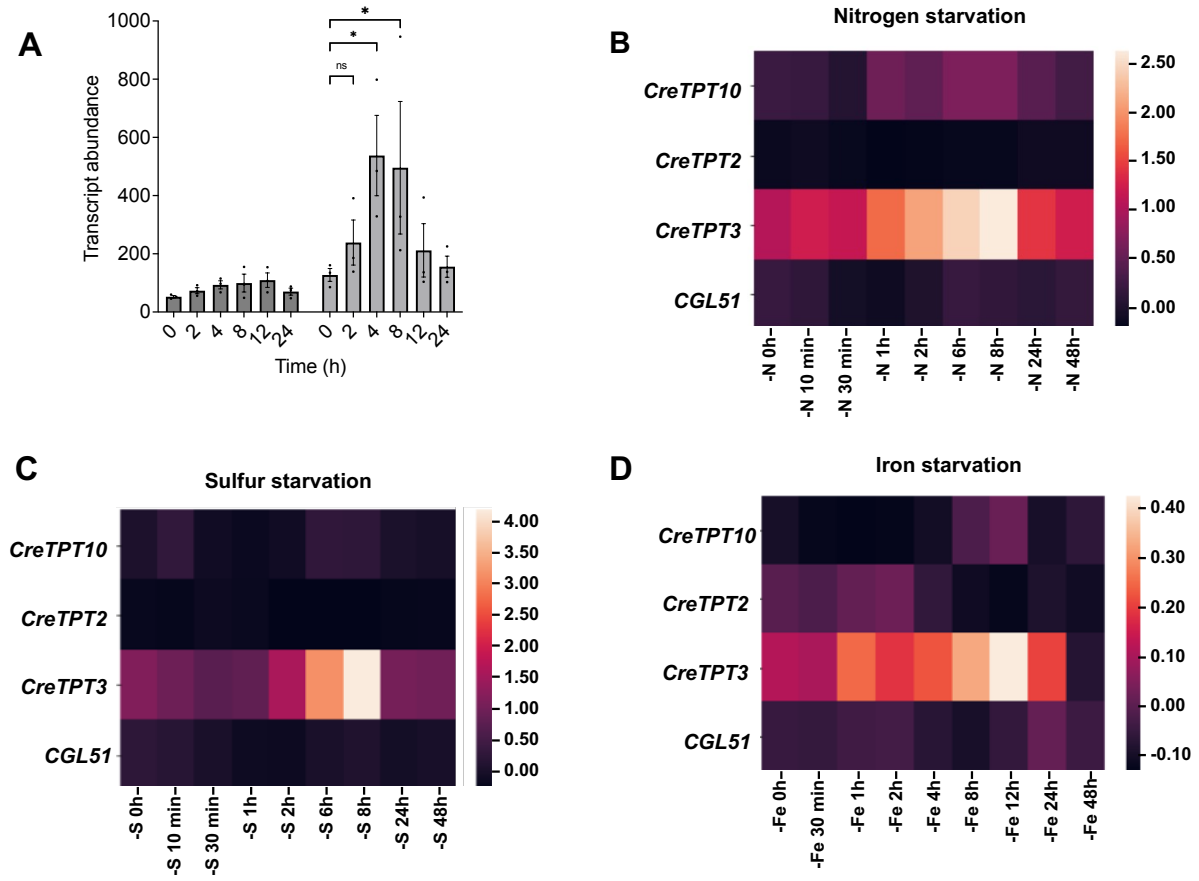

Supplementary Fig. 9: transcript changes of Cre*TPT2* and Cre*TPT3* with various conditions. **(A)** Expressions of Cre*TPT2* and Cre*TPT3* following exposure of LL grown cells to HL. Expression of the putative pPTs under nitrogen starvation **(B)**, sulfur starvation **(C)**, and iron starvation **(D)** from (Ngan et al., 2015; González-Ballester et al., 2010; Urzica et al., 2013). Supports Fig. 5,6,7.

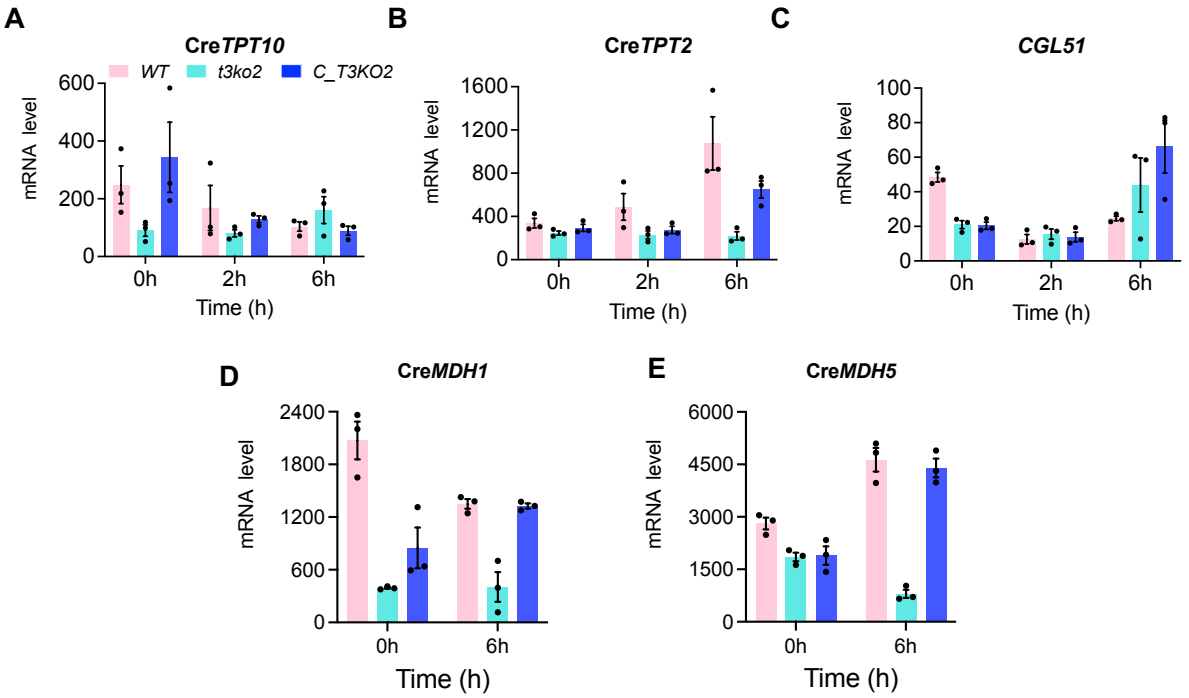

Supplementary Fig. 10: mRNA levels of Cre*TPT10* (**A**), Cre*TPT2* (**B**) and *CGL51* (**C**) in the indicated strains 0, 2, 6 h after the cells were shifted from LL to ML. (**D, E**) mRNA levels of plastidial malate dehydrogenases (*MDH*) in the indicated strains 0, 6 h after the cells were shifted from LL to ML. Supports Fig. 7.

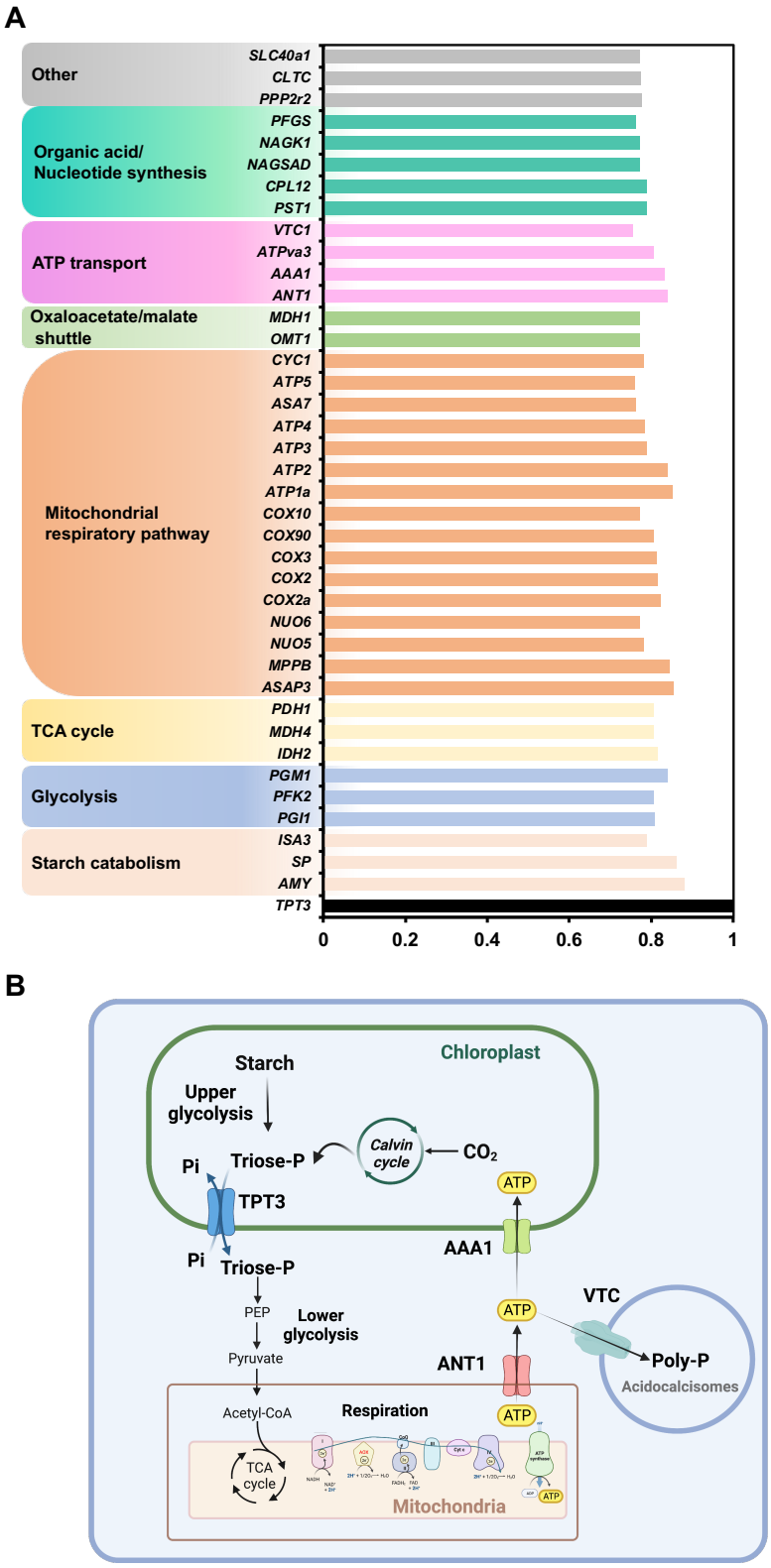

Supplementary Fig 11: List of genes with strong correlation relative to Cre*TPT3*. (**A**) Correlation coefficients greater than 0.75 were listed. (**B**) Construction of Cre*TPT3* co-expression networks. Supports Fig. 7 and 8.